



DIPLOMARBEIT

Absolute Quantifizierung von Lebermetaboliten mittels lokalisierter ^{31}P -MR-Spektroskopie bei 7 T

ausgeführt am

Atominstitut

der Technischen Universität Wien

unter der Anleitung von

Univ.Prof. Dr.techn. Gerald Badurek

in Zusammenarbeit mit

Assoc.Prof. Mag. Dr. Martin Krššák

**Exzellenzzentrum für Hochfeld-Magnetresonanz,
Universitätsklinik für Radiologie und Nuklearmedizin**

Medizinischen Universität Wien

durch

Lorenz Pflieger

Uhlandgasse 8/7

1100 Wien

Wien, 27. Oktober 2015

(Unterschrift Verfasser)



TECHNISCHE
UNIVERSITÄT
WIEN
Vienna University of Technology

(Signature of Advisor)

MASTERS'S THESIS

Absolute quantification of hepatic metabolites using localized ^{31}P -MR-spectroscopy at 7 T

performed at the
Atominstitut
of the Technische Universität Wien

under the guidance of
Univ.Prof. Dr.techn. Gerald Badurek

in cooperation with
Assoc.Prof. Mag. Dr. Martin Krššák

MR Center of Excellence,
Department of Biomedical Imaging and Image-guided Therapy
Medical University of Vienna

by

Lorenz Pflieger

Uhlandgasse 8/7
1100 Wien

Vienna, 27. Oktober 2015

(Signature of Author)

Erklärung zur Verfassung der Arbeit

Lorenz Pfleger
Uhlandgasse 8/7, 1100 Wien

Hiermit erkläre ich, dass ich diese Arbeit selbständig verfasst habe, dass ich die verwendeten Quellen und Hilfsmittel vollständig angegeben habe und dass ich die Stellen der Arbeit – einschließlich Tabellen und Abbildungen –, die anderen Werken oder dem Internet im Wortlaut oder dem Sinn nach entnommen sind, auf jeden Fall unter Angabe der Quelle als Entlehnung kenntlich gemacht habe.

(Ort, Datum)

(Unterschrift Verfasser)

Acknowledgements

First of all I want to thank my supervisor at the MR center, Assoc. Prof. Mag. Dr. Martin Krššák, for his guidance and patience through this thesis. His support and the assistance of the colleagues PhD Mag. Marek Chmelík and Mag. Martin Gajdošík were a great help whenever problems arose. I am also grateful that Marek Chmelík provided me the source code of his software tool for adaptations and I am much obliged to Martin Gajdošík for supporting me for the measurements. Furthermore, I appreciate the straight forward and uncomplicated supervision of Univ. Prof. Dr. Gerald Badurek on the part of the Technische Universität Wien. Additional acknowledgement is hereby expressed to the volunteers participating in my experiments and also to all the colleagues at the MR center for making it a comfortable working atmosphere.

Last but not least I want to thank my parents for making it possible for me to study in Vienna due to their financial support and I am also grateful for the moral support of my siblings and close friends during stressful times.

Abstract

Metabolic dysfunctions of the liver manifest as change in concentration of intracellular metabolites. An analysis of the distribution of metabolic products contributes to the understanding of liver disorders on molecular basis and could improve the therapy. By means of the 7 T whole-body MRI system of the Medical University of Vienna this thesis presents a non-invasive way to determine the local concentration of metabolites of the liver such as phosphorus compounds. Therefore healthy volunteers are examined and the distribution of certain metabolites is analyzed with the help of a phantom of known concentration. For further studies, these data could then serve as basis of comparison in order to diagnose patients with metabolic dysfunctions of the liver more precisely.

Kurzfassung

Stoffwechselstörungen der Leber äußern sich durch Konzentrationsänderung intrazellulärer Metaboliten. Eine Analyse der Verteilung von Stoffwechselprodukten trägt zum besseren Verständnis von Lebererkrankungen auf molekularer Basis bei und könnte die Therapie verbessern. Mittels des 7 T-MR-Ganzkörpertomographen des AKH Wien wird in dieser Arbeit eine nichtinvasive Möglichkeit vorgestellt, die Konzentration von Stoffwechselprodukten der Leber wie Phosphorverbindungen lokal zu bestimmen. Dazu werden gesunde Probanden untersucht und die Verteilung bestimmter Stoffwechselprodukte wird unter Zuhilfenahme eines Phantoms bekannter Konzentration analysiert. Für weitere Studien könnten diese Daten dann als Vergleichsgrundlage dienen, um Patienten mit Stoffwechselstörungen der Leber genauer zu diagnostizieren.

Acronyms

bold symbols	vectors (e. g.: \mathbf{v})
<i>italic symbols</i>	scalar variables, vector components or constants (e. g.: s)
\mathbf{B}_0	stationary external magnetic field
$\mathbf{B}_1^{(+/-)}$	magnetic RF field, perpendicular to \mathbf{B}_0 (transmitted(+)/received(-))
T_1	longitudinal or spin-lattice relaxation time
$T_2^{(*)}$	(effective) transverse or spin-spin relaxation time
T_E	Echo Time
T_I	Inversion Time
T_R	Repetition Time
δ	chemical shift
γ	gyromagnetic ratio
ν_0	Larmor frequency
σ	shielding or screening constant
$\hat{x}, \hat{y}, \hat{z}$	unity vectors in x -, y - or z -direction
^{31}P	Phosphorus-31
AHP2500	Adiabatic Half-Passage pulse, pulse length: 2500 μs
AHP3000	Adiabatic Half-Passage pulse, pulse length: 3000 μs
AMARES	Advanced Method for Accurate, Robust, and Efficient Spectral fitting
ATP	Adenosine Triphosphate
CSI	Chemical Shift Imaging
FID	Free Induction Decay
FOV	Field Of View
FWHM	Full Width at Half Maximum

GPC	Glycerophosphorylcholine
GPE	Glycerophosphorylethanolamine
jMRUI	Java-based Magnetic Resonance User Interface
MRI	Magnetic Resonance Imaging
(MR)SI	(Magnetic Resonance) Spectroscopic Imaging
MRS	Magnetic Resonance Spectroscopy
NADH	Nicotinamide Adenine Dinucleotide
NMR	Nuclear Magnetic Resonance
PC	Phosphocholine
PCr	Phosphocreatine
PDE	Phosphodiesterases
PE	Phosphoethanolamine
P _i	inorganic Phosphate
PME	Phosphomonoesters
PSF	Point Spread Function
PtdC	Phosphatidylcholine
RECT600	Rectangular pulse, pulse length: 600 μs
RF	Radio Frequency
SNR	Signal-to-Noise Ratio
SVS	Single Voxel Spectroscopy
UDPG	Uridine Diphosphoglucose
VOI	Volume Of Interest

Contents

1	Basic Principles	1
1.1	Introduction	1
1.2	Principles of Magnetic Resonance	2
1.2.1	Magnetic Spins	2
1.2.2	Interaction with RF-Fields	7
1.2.3	Bloch Equations & Relaxation	8
1.2.4	Pulse Sequences	11
1.3	Principles of MR-Spectroscopy	12
1.3.1	Chemical Shift	12
1.3.2	Localization	12
1.3.3	Spatial Resolution	13
1.3.4	³¹ P NMR Spectroscopy	13
1.4	Quantification	15
1.4.1	Metabolite Quantification in vivo	15
1.4.2	Surface Coils	16
1.4.3	³¹ P MRS in Liver	17
1.5	Aims	18
2	Materials & Methods	19
2.1	Materials & Volunteers	19
2.1.1	MR Scanner & Surface Coil	19
2.1.2	Phantoms	20
2.1.3	Volunteers	21
2.2	Methods	22
2.2.1	Experimental Setups	22
2.2.2	MR Protocols	22
2.2.3	Workflow & Postprocessing	26
2.2.4	IDL Tool Adaptions	28
3	Results	29
3.1	Preparations	29
3.1.1	T ₁ Determination	29
3.1.2	Pulse Adjustment	29

3.1.3	Positioning of the Calibration Reference	31
3.2	Absolute Quantification	34
3.2.1	Phantom Validation	34
3.2.2	Hamming Filter	35
3.2.3	Quantification Results in Vivo	35
4	Discussion	41
4.1	Preparations	41
4.1.1	T ₁ Determination	41
4.1.2	Pulse Adjustment	41
4.1.3	Positioning of the Calibration Reference	42
4.2	Absolute Quantification	44
4.2.1	Phantom Testing	44
4.2.2	Hamming Filter	44
4.2.3	Quantification Results in Vivo	45
5	Summary & Conclusion	47
A	Detailed Results	49
	Bibliography	51
	List of Figures	53
	List of Tables	54

Basic Principles

1.1 Introduction

Magnetic resonance imaging (MRI) and spectroscopy (MRS) are relative new techniques used for in vivo examinations. The basic principle behind it is the nuclear magnetic resonance (NMR) effect which was discovered in 1946 by Felix Bloch and Edward M. Purcell independently. They were awarded the Nobel Prize in Physics in 1952 for their research. In the early 1970s experiments showed that utilizing NMR is not only a technique for physicists and chemists to study magnetic moments of atoms and molecules but it can also be used in medicine for distinguishing between tissues due to its different composition of atoms and molecules. Using this and introducing localization methods, Paul C. Lauterbur and Sir Peter Mansfield laid the foundation for MRI and were honored with the Nobel Prize in Medicine in 2003 [1].

1.2 Principles of Magnetic Resonance

1.2.1 Magnetic Spins

Classical Mechanics

To explain NMR from scratch it is important to understand the classical description of a spinning object and then merge into quantum mechanic spins for details where classical physics reaches its limits.

A moving object with mass m and velocity \mathbf{v} has a linear momentum \mathbf{p} given by:

$$\mathbf{p} = m\mathbf{v} \quad (1.1)$$

According to Newton's second law, this object will continuously move on with its momentum until an external force \mathbf{F} is applied to change it:

$$\mathbf{F} = \frac{d\mathbf{p}}{dt} = m\mathbf{a} \quad (1.2)$$

where \mathbf{a} is the acceleration acting on the object [1].

If we consider instead of a linear movement a rotation with constant velocity around a fixed point in distance \mathbf{r} we get an angular momentum \mathbf{L} with:

$$\mathbf{L} = \mathbf{r} \times \mathbf{p} \quad (1.3)$$

\mathbf{L} is a vector with magnitude $m|\mathbf{v}||\mathbf{r}|$ perpendicular to the plane of motion¹. Analogous to the linear momentum, the angular momentum is only changed if an external force is applied. A useful parameter for an angular force is the torque \mathbf{T} which is defined by:

$$\mathbf{T} = \mathbf{r} \times \mathbf{F} = \mathbf{r} \times \frac{d\mathbf{p}}{dt} = \frac{d\mathbf{L}}{dt} \quad (1.4)$$

If the object has an electrical charge it generates due to its rotation a magnetic moment since it can be seen as current flowing in a loop. Its magnitude computes out of the current times the area the loop encircles. That means that an object with mass m and charge e rotating around a fixed point in distance \mathbf{r} with velocity \mathbf{v} has a magnetic moment $\boldsymbol{\mu}$ according to:

$$\boldsymbol{\mu} = \frac{e\mathbf{v}}{2\pi|\mathbf{r}|}\pi|\mathbf{r}|^2 \quad (1.5)$$

Substituting with $\mathbf{L} = m\mathbf{v}\mathbf{r}$ results in:

$$\boldsymbol{\mu} = \frac{e}{2m}\mathbf{L} = \gamma\mathbf{L} \quad (1.6)$$

with γ being the so called gyromagnetic ratio. If this charged rotating object is now in an external magnetic field \mathbf{B}_0 the torque acting on it is calculated by:

$$\mathbf{T} = \boldsymbol{\mu} \times \mathbf{B}_0 \quad (1.7)$$

¹considering that \mathbf{r} and \mathbf{p} are perpendicular to each other

Taking the equations (1.4), (1.6) and (1.7) into account we get the following:

$$\frac{d\boldsymbol{\mu}}{dt} = \gamma\boldsymbol{\mu} \times \mathbf{B}_0 \quad (1.8)$$

The absolute value of the magnetic moment $|\boldsymbol{\mu}|$ does not change over time therefore the differential equation (1.8) implies that $\boldsymbol{\mu}$ changes its direction over time, i. e. it precesses around \mathbf{B}_0 . Hence the equation can be rewritten as:

$$\frac{d\boldsymbol{\mu}}{dt} = \boldsymbol{\mu} \times \boldsymbol{\omega}_0 \quad (1.9)$$

These two differential equations (1.8) and (1.9) result in the angular velocity $\boldsymbol{\omega}_0 = \gamma\mathbf{B}_0$ and subsequently the precession frequency ν_0 is defined by:

$$\nu_0 = \frac{|\boldsymbol{\omega}_0|}{2\pi} = \frac{\gamma}{2\pi} |\mathbf{B}_0| \quad (1.10)$$

ν_0 is also called Larmor frequency and is directly proportional to the external field \mathbf{B}_0 and the gyromagnetic ratio γ , which is specific for the observed object, e. g. a spinning nucleus [1].

Depending on its orientation in the applied magnetic field, magnetic energy E is attributed to the magnetic moment with:

$$E = -\boldsymbol{\mu} \cdot \mathbf{B}_0 = -|\boldsymbol{\mu}| |\mathbf{B}_0| \cos \theta \quad (1.11)$$

where θ is the angle between the magnetic moment $\boldsymbol{\mu}$ and external magnetic field \mathbf{B}_0 . So the magnetic energy is at a minimum when both $\boldsymbol{\mu}$ and \mathbf{B}_0 are parallel to each other ($\theta = 0^\circ$) and maximized when they are anti-parallel ($\theta = 180^\circ$). In classical physics $\boldsymbol{\mu}$ and \mathbf{B}_0 could align along any orientation to each other ($0^\circ \leq \theta \leq 180^\circ$) meaning that the magnetic energy can take any value in between $-|\boldsymbol{\mu}| |\mathbf{B}_0|$ and $+|\boldsymbol{\mu}| |\mathbf{B}_0|$. From here on a quantum mechanic point of view is necessary since there is no continuous energy distribution possible but rather quantized with steps of $\Delta E = h\nu$ [1].

Quantum Mechanics

In quantum mechanics the angular momentum \mathbf{L} of spinning elementary particles is assumed to take only certain values according to:

$$|\mathbf{L}| = \hbar\sqrt{I(I+1)} \quad (1.12)$$

I is the so called spin quantum number and has integral or half-integral values and \hbar is equal $h/2\pi$ with h being the Planck's constant ($\approx 6.626 \cdot 10^{-34}$ Js). For a complete characterization of \mathbf{L} its direction needs to be specified additionally. This is described by the magnetic quantum number m (from now on m is no more referred to as the mass). The component of the angular momentum along z -direction L_z of a coordinate system (x, y, z) is then given by:

$$L_z = \hbar m \quad (1.13)$$

That means that m can take $2I + 1$ values with $m = -I, -I + 1, \dots, I - 1, I$. The spin quantum number I is particle specific and is e. g. for protons, neutrons and electrons equal $\frac{1}{2}$. For other particles I behaves according to the following rules depending on the atomic mass and the charge:

- nuclei with odd mass number: I is half-integral value
($\frac{1}{2}, \frac{3}{2}, \frac{5}{2}, \dots$; e. g. $^1\text{H}, ^{13}\text{C}, ^{15}\text{N}, ^{17}\text{O}, ^{23}\text{Na}, ^{31}\text{P}$)
- nuclei with even mass number and even charge number: I is zero
e. g. $^{12}\text{C}, ^{16}\text{O}, ^{32}\text{S}$)
- nuclei with even mass number and odd charge number: I is integral value
1, 2, 3, ...; e. g. $^2\text{H}, ^{14}\text{N}$)

Analogous to the classical description, also in a quantum mechanical point of view particles can be characterized with a magnetic moment $\boldsymbol{\mu}$ by means of equation (1.6):

$$\boldsymbol{\mu} = \gamma \mathbf{L} \quad (1.14)$$

where γ is again the gyromagnetic ratio². Since the angular momentum \mathbf{L} is quantized, the same is valid for the magnetic moment $\boldsymbol{\mu}$ and a component along z -direction (in analogy to equation (1.13)) is given by:

$$\mu_z = \gamma \hbar m \quad (1.15)$$

By applying an external magnetic field \mathbf{B}_0 along z -direction according to equation (1.11) the magnetic energy E results in:

$$E = -\mu_z |\mathbf{B}_0| = -\gamma \hbar m |\mathbf{B}_0| \quad (1.16)$$

Because of the quantized nature of m also the magnetic energy is quantized. For particles with I equal $\frac{1}{2}$ there are only two energy levels possible with $m = \pm \frac{1}{2}$. The energy difference ΔE is then given by:

$$\Delta E = \gamma \hbar |\mathbf{B}_0| \quad (1.17)$$

This equation is valid for any neighboring energy levels since these differ in m by 1 (and is called nuclear Zeeman effect). To change the energy state to an adjacent energy level an oscillating magnetic field \mathbf{B}_1 has to be applied in the xy -plane which fulfills the condition:

$$\Delta E = h\nu_0 \quad (1.18)$$

with:

$$\nu_0 = \frac{\gamma}{2\pi} |\mathbf{B}_0| \quad (1.19)$$

ν_0 is again the Larmor frequency. Although both approaches yield in the same result, only the quantum mechanic point of view describes the NMR effect in a quantitative way. Though, in a macroscopic system the classical description of subsection 1.2.1 helps to understand the magnetization of spin ensembles as is shown in the next subsection [1, 2].

²unlike the classical definition in equation (1.6) in quantum mechanics the gyromagnetic ratio γ has another particle dependent factor, the so called g-factor included

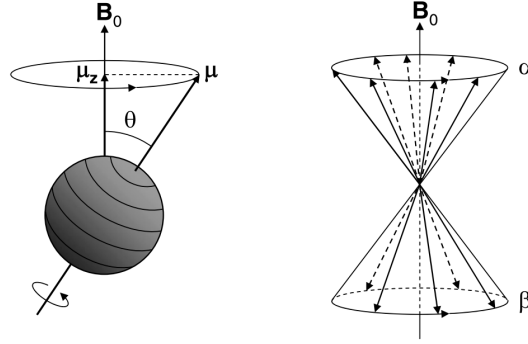


Figure 1.1: Left: precession of sphere with magnetic moment μ in an external magnetic field \mathbf{B}_0 with angle θ ; right: magnetic moments of a spin ensemble ($I = 1/2$) spanning two cones and distributing by means of the Boltzmann equation (1.21) to their α and β states [1].

Macroscopic Magnetization

Figure 1.1, left depicts the classical description of a precessing magnetic moment in an external magnetic field. Considering the quantization of the quantum mechanics there are only certain angles θ allowed between μ and \mathbf{B}_0 which follow the condition:

$$\cos \theta = \frac{m}{\sqrt{I(I+1)}} \quad (1.20)$$

Assuming a nucleus with I equal $1/2$ (e. g. a proton) the angle of the magnetic moment will be around 54.74° with respect to the z -axis. These two states are often referred to as α (μ parallel to \mathbf{B}_0) and β spin states (μ anti-parallel to \mathbf{B}_0). The magnetic moments will span two cones with the calculated angle rotating with the Larmor frequency about the magnetic field \mathbf{B}_0 (Figure 1.1, right). For any possible number of I the magnetic moments will be distributed on $2I + 1$ cones each with an angle according to equation (1.20) [1].

In a macroscopic volume the Boltzmann equation describes the ratio of the population of the two energy states of Figure 1.1, right:

$$\frac{n_\alpha}{n_\beta} = e^{\Delta E/kT} = e^{h\nu/kT} \quad (1.21)$$

with $n_{\alpha/\beta}$ as the number of spins in α/β -state, k as the Boltzmann constant ($\approx 1.381 \cdot 10^{-23}$ J/K) and T as the absolute temperature. At temperatures of a few $^\circ\text{C}$ and magnetic field strength of a few T, the magnetic energy difference ΔE for nuclei is much less than the thermal energy kT . Therefore we can approximate the Boltzmann equation (1.21) with its first-order Taylor series:

$$\frac{n_\alpha}{n_\beta} \approx 1 + \frac{h\nu}{kT} \quad (1.22)$$

Under in vivo conditions with a temperature of 37°C (310.15 K) and an applied static magnetic field of 7 T the population difference between the two states for protons ($\gamma \approx 2.675 \cdot 10^8$ rad/sT \Rightarrow

Table 1.1: Characteristics of a few nuclei used for in vivo NMR [1, 3].

Isotope	Spin I	Gyromagnetic ratio γ [10^6 rad/sT]	NMR frequency $\nu/ \mathbf{B}_0 $ [MHz/T]	Natural abundance [%]	Relative sensitivity ³
¹ H	$\frac{1}{2}$	267.513	42.576	99.985	1.00
¹³ C	$\frac{1}{2}$	67.261	10.705	1.108	$1.76 \cdot 10^{-4}$
¹⁷ O	$\frac{5}{2}$	-36.264	-5.772	0.037	$1.08 \cdot 10^{-5}$
²³ Na	$\frac{3}{2}$	70.761	11.262	100.000	$9.25 \cdot 10^{-2}$
³¹ P	$\frac{1}{2}$	108.291	17.235	100.000	$6.63 \cdot 10^{-2}$

$\nu \approx 298$ MHz at 7 T) will be only 0.0023 % (i. e. in one million protons will be just 23 spins more in α -state than in β -state) [1, 2].

The magnetization \mathbf{M} of a spin ensemble is composed of the sum of the single magnetic moments of all the spins. The spins are randomly distributed on each spin state which means that the net component of the magnetization in the xy -plane cancels out to zero (Figure 1.1, right). The remaining component of \mathbf{M} is parallel to \mathbf{B}_0 and results from the population difference between the single spin states. At thermal equilibrium this longitudinal magnetization, termed by \mathbf{M}_0 is given by:

$$|\mathbf{M}_0| = \left| \sum_{i=1}^n \boldsymbol{\mu}_i \right| = n_\alpha \mu_{z\alpha} + n_\beta \mu_{z\beta} = \gamma \frac{\hbar}{2} (n_\alpha - n_\beta) \quad (1.23)$$

with $n = n_\alpha + n_\beta$ as the total number of spins of the ensemble. Combining this with equation (1.22) and $h\nu/kT \ll 1$ the population difference $n_\alpha - n_\beta$ is given by:

$$n_\alpha - n_\beta \approx \frac{nh\nu}{2kT} \quad (1.24)$$

Over all the equations (1.23) and (1.24) result in:

$$|\mathbf{M}_0| \approx (\gamma\hbar)^2 \frac{n |\mathbf{B}_0|}{4kT} \quad (1.25)$$

This approximation indicates that the magnetization is dependent on the square of the gyromagnetic ratio of the studied nucleus, on the number of those nuclei in the sample, on the external magnetic field and inverse on the temperature. The latter dependence is also known as Curie's law. For in vivo investigations a change in temperature is non-applicable. Therefore the linear dependence of \mathbf{M}_0 on \mathbf{B}_0 cause a trend towards higher magnetic field strength in medical NMR applications (nowadays 3 T is the standard for clinical scanners, whereas for human in vivo research magnetic field strengths reach up to 11.7 T) [1].

Factors influencing the sensitivity are beneath the above mentioned also natural abundance of the nucleus under investigation, noise and relaxation parameters. Depending on what is examined, the sensitivity is already partly specified by the studied nucleus (gyromagnetic ratio and

³relative sensitivity to ¹H, proportional to $|\gamma|^3 |I(I+1)|$ times the natural abundance

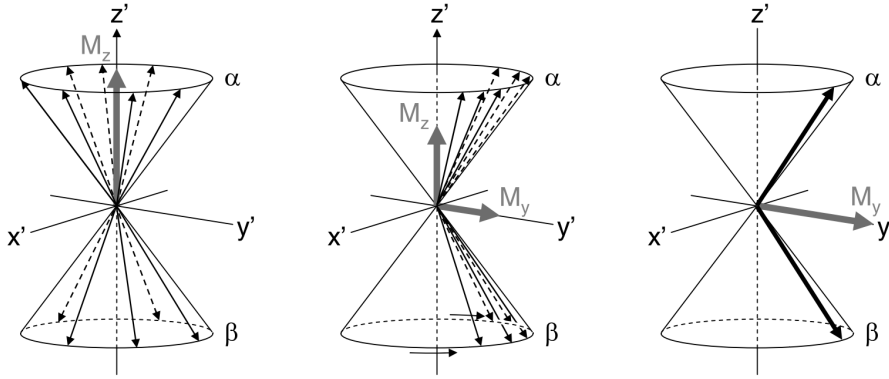


Figure 1.2: Spin ensemble in a rotating frame (x' , y' , z' , with $z' = z$); left: thermal equilibrium with only \mathbf{B}_0 along positive z , resulting magnetization M_z parallel to \mathbf{B}_0 ; middle: additionally applied \mathbf{B}_1 rotating with the frame: spin states getting more equally distributed and spins getting more in phase; right: final equal distribution in the spin states and spins precessing totally in phase: resulting magnetization M_y rotating perpendicular to \mathbf{B}_0 [1].

natural abundance), its relative abundance in biological tissues and the volume of interest (VOI). Table 1.1 shows some NMR relevant characteristics of commonly used nuclei for in vivo NMR [1].

1.2.2 Interaction with RF-Fields

In a stationary external magnetic field, the magnetic moments of nuclear spins are precessing around this magnetic field as explained in subsection 1.2.1 (see also Figure 1.1, left). The sum of these moments build up the total net magnetization \mathbf{M}_0 and can be treated according to the classical description. For a change of \mathbf{M}_0 , the population distribution among the spin states and the coherence of the precession can be influenced. This is achieved by applying an oscillating field \mathbf{B}_1 in the transverse xy -plane fulfilling the condition of equation (1.18) as already mentioned in subsection 1.2.1 Quantum Mechanics. Actually \mathbf{B}_1 is not a continuous wave but a radio frequency (RF) pulse (MHz range, see Table 1.1, NMR frequency) long enough to achieve the aimed state. Assuming \mathbf{B}_1 such that \mathbf{M}_0 gets totally flipped into the transverse plane (xy -plane), means that α - and β -states are equally populated and the spins rotate phase coherently as visualized in Figure 1.2. This pulse is then called 90° -pulse since it changes the direction of the total net magnetization about 90° . This resulting magnetization gives rise to a NMR signal in a receiver coil, since its rotation induces an electrical current in the coil [1].

1.2.3 Bloch Equations & Relaxation

Generalizing equation (1.8) with $\mathbf{M}(t)$ being the time dependent sum over all single magnetic moments of the spins results in:

$$\frac{d\mathbf{M}(t)}{dt} = \mathbf{M}(t) \times \gamma \mathbf{B}(t) \quad (1.26)$$

where $\mathbf{B}(t)$ is the time dependent total external magnetic field, containing the stationary field \mathbf{B}_0 in the z -component and the oscillating field \mathbf{B}_1 in the x - and y -component. In thermal equilibrium without an oscillating field applied ($\mathbf{B}_1 = 0$) the z -component of the magnetization does not change over time:

$$\frac{dM_z(t)}{dt} = 0 \quad (1.27)$$

In this configuration both the x - and y -component of \mathbf{M} are zero and no NMR signal can be detected. To get a signal the z -component needs to be flipped in the xy -plane so it can induce current in the receiver coil through its oscillation. This is achieved by a time dependent \mathbf{B}_1 -field linearly polarized along the x -axis:

$$\mathbf{B}_1(t) = 2B_1 \cos(\omega t) \hat{\mathbf{x}} \quad (1.28)$$

where B_1 is the maximum amplitude and ω is angular transmitter or carrier frequency of the applied RF field and $\hat{\mathbf{x}}$ is a unity vector along the x -axis. Equation (1.28) can be rewritten as a linear combination of two counter rotating circularly polarized fields:

$$\mathbf{B}_1(t) = B_1 (\cos(\omega t) \hat{\mathbf{x}} + \sin(\omega t) \hat{\mathbf{y}}) + B_1 (\cos(\omega t) \hat{\mathbf{x}} - \sin(\omega t) \hat{\mathbf{y}}) \quad (1.29)$$

Thereby only the field rotating in the same direction as the magnetic moments takes a significant influence on the magnetic moments. The counter rotating field interacts on the spins with a value in the order of $(B_1/2B_0)^2$. This is called the Bloch-Siegert shift and is typically a very small number and therefore negligible. Thus \mathbf{B}_1 is approximated by:

$$\mathbf{B}_1(t) = B_1 (\cos(\omega t) \hat{\mathbf{x}} - \sin(\omega t) \hat{\mathbf{y}}) = \begin{pmatrix} B_1 \cos(\omega t) \\ -B_1 \sin(\omega t) \\ 0 \end{pmatrix} \quad (1.30)$$

The transformation between the laboratory frame of reference and a rotating frame (indicated by a prime) with angular velocity ω can be described by a matrix multiplication by a rotation matrix \mathcal{R} :

$$\mathbf{B}' = \mathcal{R}\mathbf{B} = \begin{pmatrix} \cos(\omega t) & \sin(\omega t) & 0 \\ -\sin(\omega t) & \cos(\omega t) & 0 \\ 0 & 0 & 1 \end{pmatrix} \begin{pmatrix} B_{1x} \\ B_{1y} \\ B_0 \end{pmatrix} \quad (1.31)$$

From equation (1.26) with the $\mathbf{B}(t)$ containing \mathbf{B}_1 in the xy -plane and \mathbf{B}_0 as the z -component as described earlier, the Bloch equations in the laboratory frame without relaxation can be derived

according to:

$$\frac{dM_x(t)}{dt} = \gamma (M_y(t)B_0 - M_z(t)B_{1y}) \quad (1.32)$$

$$\frac{dM_y(t)}{dt} = \gamma (M_z(t)B_{1x} - M_x(t)B_0) \quad (1.33)$$

$$\frac{dM_z(t)}{dt} = \gamma (M_x(t)B_{1y} - M_y(t)B_{1x}) \quad (1.34)$$

A system will always try to reach the state of thermal equilibrium. After a perturbation this process is called relaxation and since it shows exponential decay it may be described by differential equations of the form:

$$\frac{dM_x(t)}{dt} = -\frac{M_x(t)}{T_2} \quad (1.35)$$

$$\frac{dM_y(t)}{dt} = -\frac{M_y(t)}{T_2} \quad (1.36)$$

$$\frac{dM_z(t)}{dt} = -\frac{M_z(t) - M_0}{T_1} \quad (1.37)$$

with the time constants T_1 and T_2 . The reason for two different time constants is that there are different relaxation effects. The longitudinal or spin-lattice relaxation time T_1 describes the return of the magnetization in z -direction to its thermal equilibrium state M_0 , regarding to the initial population of the different spin states. Thereby, energy is transferred to the surrounding, referred to as lattice. T_2 is the transverse or spin-spin relaxation time and describes the fading of the transverse magnetization due to the loss of phase coherence of the precessing spins. This means an increase of the systems' entropy since the spins exchange energy only among themselves and the total energy is conserved. Actually, the effective transverse relaxation time which is measured is smaller than T_2 , resulting from inhomogeneity in the magnetic field and is referred to as T_2^* . The spin-lattice relaxation time is longer than the spin-spin relaxation time because the initial magnetization is only reached after the transverse component of the magnetization is vanished. The complete Bloch equations in a laboratory frame of reference are then given by combining equations (1.32)–(1.37):

$$\frac{dM_x(t)}{dt} = \gamma (M_y(t)B_0 - M_z(t)B_{1y}) - \frac{M_x(t)}{T_2} \quad (1.38)$$

$$\frac{dM_y(t)}{dt} = \gamma (M_z(t)B_{1x} - M_x(t)B_0) - \frac{M_y(t)}{T_2} \quad (1.39)$$

$$\frac{dM_z(t)}{dt} = \gamma (M_x(t)B_{1y} - M_y(t)B_{1x}) - \frac{M_z(t) - M_0}{T_1} \quad (1.40)$$

Analogous to equation (1.31) the magnetization can be as well transformed to a rotating frame.

The Bloch equations (1.38)–(1.40) in a rotating frame are then given by:

$$\frac{dM'_x(t)}{dt} = -(\omega_0 - \omega) M'_y(t) - \gamma B'_{1y} M'_z(t) - \frac{M'_x(t)}{T_2} \quad (1.41)$$

$$\frac{dM'_y(t)}{dt} = (\omega_0 - \omega) M'_x(t) + \gamma B'_{1x} M'_z(t) - \frac{M'_y(t)}{T_2} \quad (1.42)$$

$$\frac{dM'_z(t)}{dt} = \gamma B'_{1y} M'_x(t) - \gamma B'_{1x} M'_y(t) - \frac{M'_z(t) - M_0}{T_1} \quad (1.43)$$

Considering the initial definition of $\mathbf{B}_1(t)$ of equation (1.30) in a rotating frame it will appear static with only the x -component being nonzero with $B'_{1x} = B_1$. Therefore the Bloch equations in such a rotating frame of reference reduce to:

$$\frac{dM'_x(t)}{dt} = -(\omega_0 - \omega) M'_y(t) - \frac{M'_x(t)}{T_2} \quad (1.44)$$

$$\frac{dM'_y(t)}{dt} = (\omega_0 - \omega) M'_x(t) + \gamma B_1 M'_z(t) - \frac{M'_y(t)}{T_2} \quad (1.45)$$

$$\frac{dM'_z(t)}{dt} = -\gamma B_1 M'_y(t) - \frac{M'_z(t) - M_0}{T_1} \quad (1.46)$$

Since only the rotating frame of reference is taken into account from now on the prime of the variables will be omitted. Equations (1.41)–(1.46) indicate that the magnetization seems to precess with a reduced value of $\omega_0 - \omega$. Therefore an effective field \mathbf{B}_e can be defined around which the magnetization precesses with a magnitude of:

$$|\mathbf{B}_e| = \sqrt{|\mathbf{B}_1|^2 + \left(\frac{\omega_0 - \omega}{\gamma}\right)^2} \quad (1.47)$$

That means that for a RF pulse on resonance (with $\omega = \omega_0$) the magnetization will only rotate about \mathbf{B}_1 since $\mathbf{B}_e = \mathbf{B}_1$ [1].

After an excitation measured components of the magnetization may behave according to:

$$M_x(t) = M_0 e^{-t/T_2^*} \cos((\omega_0 - \omega)t + \phi) \quad (1.48)$$

$$M_y(t) = M_0 e^{-t/T_2^*} \sin((\omega_0 - \omega)t + \phi) \quad (1.49)$$

$$M_z(t) = M_0 \left(1 - e^{-t/T_1}\right) \quad (1.50)$$

with ϕ as the phase at $t = 0$. This means that these equations are solutions of equations (1.44)–(1.46). A measured signal which shows such an exponential decay function is called free induction decay (FID). Figure 1.3 shows such an FID. The envelope of each component is an exponential function with its characteristic time constant. In the xy -plane the FID can be seen as complex function with $M_{xy} = M_x + iM_y$. In general, one is more interested in the spectral composition of the signal so a Fourier transformation needs to be performed:

$$F(\omega) = \int_{-\infty}^{\infty} f(t) e^{-i\omega t} dt \quad (1.51)$$

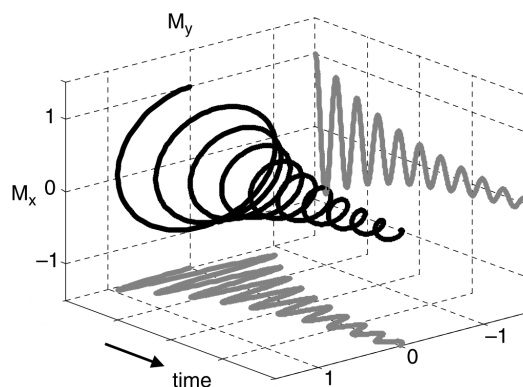


Figure 1.3: FID signal of the magnetization in the xy -plane and its components over time [1].

In the frequency domain the complex function is build up of absorption and diffusion components of Lorentzian line shapes. By post-process phase shifting the absorption components can be transferred to the real part so the diffusion remains as imaginary part. The peak of the real part represents then the height of the signal [1].

1.2.4 Pulse Sequences

For imaging there are two basic techniques: T_1 and T_2 weighted contrast. For the first one the repetition time T_R between consecutive 90° excitation pulses is chosen in a way that not all spins are back in an equilibrium state again. This spin-lattice relaxation is dependent on the tissue the spins are located and leads to different signal amplitudes referred to as saturation. Therefore, the measured signals create T_1 weighted contrast. It can be influenced by varying T_R or the flip angles of the excitation pulse to less than 90° for different saturation [2].

T_2 weighted contrast is achieved by applying a second 180° pulse after a time $T_E/2$ after a 90° excitation pulse. Since the spin-spin relaxation occurs due to dephasing in the xy -plane the 180° pulse will flip the 'dephasing direction' of the single spins leading to a refocusing after an echo time T_E . Since the spin-spin relaxation is dependent on the tissue the spins are located a T_2 weighted contrast can be gained from the measured echo signal. Both methods are combined with spatial encoding and used for imaging with T_1 or T_2 weighted contrast [2].

Another way to determinate T_1 is by inversion recovery. Therefore, a 180° excitation pulse is applied and after a inversion time T_I a 90° pulse flips the magnetization into the xy -plane for readout. Repeating this with varying T_I for each time a different relaxation state is recorded and the relaxation process can be reconstructed [2].

1.3 Principles of MR-Spectroscopy

1.3.1 Chemical Shift

The key effect that enables MR-spectroscopy is the chemical shift: The external applied magnetic field \mathbf{B}_0 has not only an effect on the nuclei, but also on the surrounding electrons. These electrons or electron clouds as referred to in quantum mechanics⁴ rotate also about \mathbf{B}_0 and therefore they are shielding the applied field according to:

$$\mathbf{B}_{\text{eff}} = \mathbf{B}_0 (1 - \sigma) \quad (1.52)$$

where \mathbf{B}_{eff} is the effective field seen by the nucleus and σ is the shielding or screening constant which is usually a very small scalar. So for isotopes in different molecules or even at different positions in one molecule the effective field might vary depending on its surrounding⁵ and furthermore the nuclei resonate at slightly different frequencies. To compare spectra achieved at various strong magnetic fields it is more convenient to scale the frequency domain in parts per million (ppm) than in absolute values. The chemical shift δ is then defined as the relative frequency distance from one reference frequency ν_0 :

$$\delta = \frac{\nu - \nu_0}{\nu_0} \cdot 10^6 \text{ [ppm]} \quad (1.53)$$

In the early time of NMR continuous waves were used for excitation instead of RF-pulses. The resonance condition was achieved by varying the field strength of the external magnetic field \mathbf{B}_0 . That means that for higher shielding the nucleus 'sees' a lower effective field and therefore needs a higher external field applied to meet the resonance condition. By convention its resonance is said to be shifted up-field, although for pulsed methods the actual NMR frequency is lower for stronger shielded nuclei. Negative chemical shifts are referred to as up-field, whereas positive chemical shifts are referred to as down-field. Traditionally negative chemical shifts are drawn right on the frequency scale and positive left [1, 2, 4].

1.3.2 Localization

In MRS, basically it can be distinguished between two localization techniques: single voxel spectroscopy (SVS) and multi voxel spectroscopy or (magnetic resonance) spectroscopic imaging ((MR)SI), e. g. chemical shift imaging (CSI). In SVS only the signal from the volume of interest (VOI) is excited. This is achieved by exciting three slices orthogonal to each other in sequence by the application of frequency selective RF pulses and \mathbf{B}_0 gradients at the same time. The remaining received signal originates then from the intersection of these three slices. For CSI the individual voxels are usually located by pulses following the RF excitation pulse or localization scheme. This is possible in one to three dimensions (1D-, 2D-, 3D-CSI). Comparing SVS with CSI both techniques have advantages and disadvantages: The most obvious difference is that in SVS only one spectrum from a certain volume is received whereas in CSI many spectra

⁴in quantum mechanics electrons are not seen as particles but rather as some kind of diffuse cloud

⁵due to different binding partners the binding electrons of the nucleus are the main source of the shielding

originating from different locations covering larger VOI can be measured. But contamination in SVS is based on RF-pulse profile whereas in CSI it is based on the point spread function (PSF, see subsection 1.3.3). Thus real voxels are larger than those prescribed and therefore overlapping each other so there is no clear separation possible which leads to some kind of blurring. SVS has usually a shorter acquisition time than CSI. Large datasets are generated in CSI which might require an automated analysis procedure [4–7].

1.3.3 Spatial Resolution

The spatial resolution in MRSI is dependent on the number of used encoding steps. The nominal voxel size is then calculated by the ratio of the field of view (FOV) and the number of encoding steps in each dimension. If a time-domain signal is not measured an infinite time but is cut off then its Fourier transformation will be a convolution of the actual frequency-domain signal and a sinc-function⁶. Due to short relaxation times compared to T_R this does not influence the spectra much, but as for spatial encoding it does matter. The Fourier transform of the spatial-domain is the so called k-space. Since the k-space sampling is limited the same effect as described for the time-domain is observable. This is then referred to as the PSF and leads to an actual broadening of the nominal voxel size and to side lobes influencing other voxels⁷ (Figure 1.4). The observed voxel size appears then around 21 % larger than the nominal voxel size and only around 87.3 % of the measured signal originates from the nominal voxel size, while the remaining 12.7 % distribute on adjacent voxels. To avoid these side lobes a weighting function can be applied on the k-space voxel grid. Therefore, one commonly used function is the Hamming filter:

$$W(k) = 0.54 + 0.46 \cos\left(\frac{\pi k}{k_{max}}\right) \quad \text{for} \quad -k_{max} \leq k \leq k_{max} \quad (1.54)$$

with k_{max} being the maximum sampled position in k-space. As already mentioned this function greatly suppresses the voxel bleeding caused by the PSF but it also leads to additional broadening of the peak and hence increasing the actual voxel size. The full width at half maximum (FWHM) of the 1D PSF gets stretched by 85 % if a Hamming filter is applied. [1].

1.3.4 ³¹P NMR Spectroscopy

Although the abundance of phosphorus-31 (³¹P) in biological systems is quite low and its gyromagnetic ratio is about 40 % of a proton, it is suitable for in vivo NMR spectroscopy. Reasons for that are its natural abundance of 100 % and its relatively large spectral range of about 30 ppm with well defined peaks. These signals arise from mobile components which play a major role in metabolism on molecular basis. Immobile phosphorus molecules such as membrane phospholipids have very broad signals and only marginal influence on the baseline. The low phosphorus concentrations result in low signal-to-noise ratio (SNR) which can be improved by using higher field strengths. Some measurable phosphorus compounds are adenosine triphosphate (ATP)

⁶ $\text{sinc } x = \frac{\sin x}{x}$

⁷known as 'voxel bleeding'

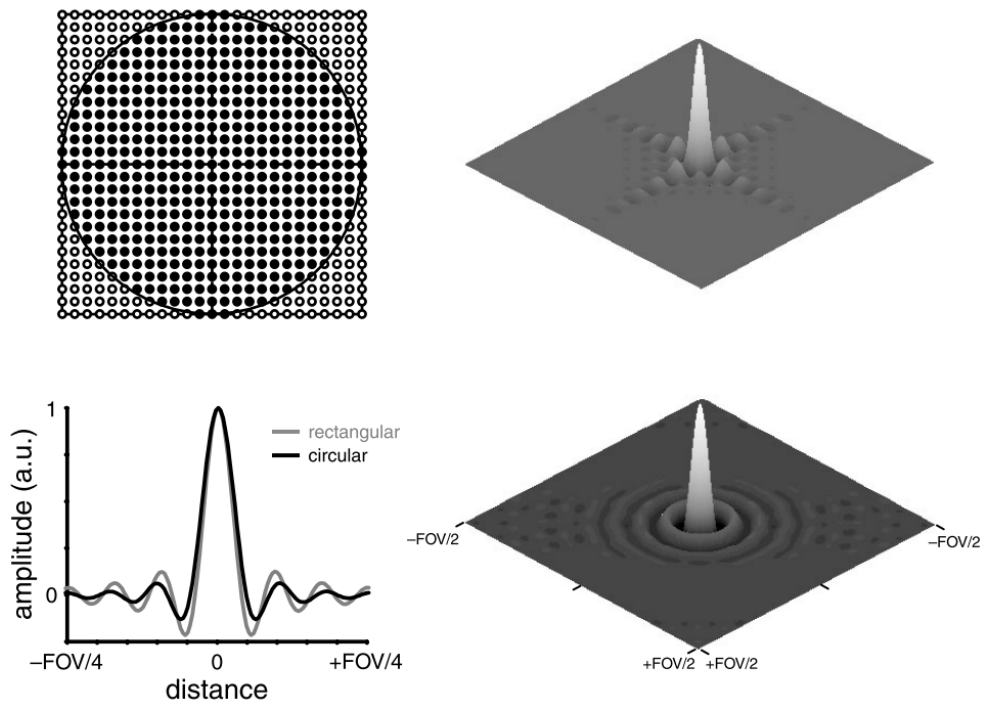


Figure 1.4: Top left: rectangular (all dots) and circular (only black dots) k-space sampling of a 25×25 grid; bottom left: 1D PSF of rectangular & circular k-space sampling; top & bottom right: 2D PSF of rectangular & circular k-space sampling [1].

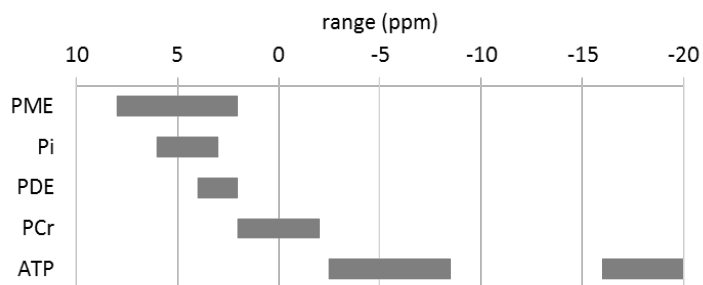


Figure 1.5: Range of ^{31}P metabolites measured with MRS, relative to PCr at pH 7 (0 ppm) [2].

with three resonances (α , β , γ), phosphocreatine (PCr), inorganic phosphate (P_i) and phosphomonoesters (PME) and phosphodiester (PDE). Figure 1.5 shows the frequency range of these metabolites, relative to PCr at a pH value of 7 (0 ppm) [2, 4].

1.4 Quantification

1.4.1 Metabolite Quantification in vivo

Figure 1.6 shows an in vivo ^{31}P NMR spectra of a human liver. The concentration of single metabolites is then proportional to the integral of the corresponding peaks fitted by Lorentzian line shapes as mentioned in the last paragraph of subsection 1.2.3. Due to possible magnetic inhomogeneity the line width might be broadened and a Gaussian function might fit the curve better. For better comparisons FWHM is used to describe line broadening [5].

There are two methods of quantification, relative and absolute quantification, which have both their advantages and disadvantages. In relative quantification ratios of concentrations of two metabolites are calculated by comparing the peak heights relative to a reference peak. Since only one spectrum is used for calculation, \mathbf{B}_1 inhomogeneity plays no role and there is no need for another reference. In contrast, absolute quantification requires a reference with known concentration to compare against. If a phantom is used⁸ to correct for the \mathbf{B}_1 inhomogeneity, its NMR signals need to be assessed in the same way and from the same position in space relative to the coil as for the in vivo measurement. This cancels out the position dependent field distribution, but does not correct for the coil load, meaning the range of the signal heights. Therefore another reference for calibration is necessary, placed in the same location relative to the coil for both in vivo and phantom measurement [4, 5].

The basis of absolute quantification is the comparison of in vivo data to phantom data with known concentration according to the following formula:

$$c_{(x,y,z)} = c_p \frac{I_{(x,y,z)}}{I_p(x,y,z)} \frac{S_p}{S} \frac{I_{ref}(p)}{I_{ref}} \quad (1.55)$$

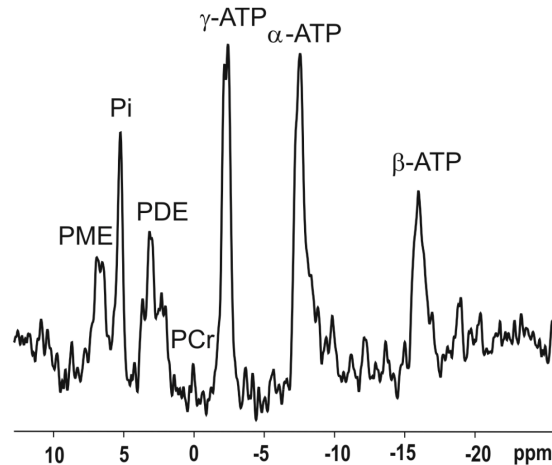


Figure 1.6: In vivo ^{31}P NMR spectrum of a human liver at 3 T [5].

⁸another option would be the use of simulation data

Table 1.2: T_1 times of some hepatic metabolites of healthy subjects at 7 T [10].

	PE	PC	P _i	GPE	GPC	γ-ATP	α-ATP	β-ATP
mean (s)	4.41	3.74	0.70	6.19	5.94	0.50	0.46	0.56
abs. SD (s)	1.55	1.31	0.33	0.91	0.73	0.08	0.07	0.07
rel. SD (%)	35.15	35.03	47.14	14.70	12.29	16.00	15.22	12.50

where $c_{(x,y,z)}$ is the absolute concentration of a metabolite of a voxel in the CSI grid with coordinates (x, y, z) , c_p the known phantom concentration, $I_{(x,y,z)}$ and $I_p(x,y,z)$ are the corresponding signal integrals at the same location, S_p and S saturation correction factors and $I_{ref(p)}$ and I_{ref} corresponding signal integrals of a calibration reference. The index p indicates that the values are acquired from the phantom data. So the B_1 inhomogeneity is corrected for by $I_p(x,y,z) \cdot S$ and S_p correct for different achieved saturations due to different T_1 times and are calculated as follows [8]:

$$S = 1 - e^{-T_R/T_1} \quad (1.56)$$

where T_R is a defined measurement parameter and T_1 times are specific for each metabolite (Table 1.2) or phantom. The latter ones have to be determined by measurements. The different coil loads are corrected by the ratio of the signal integrals of the calibration reference I_{ref} and $I_{ref(p)}$ [9].

1.4.2 Surface Coils

Surface coils are in use for ^{31}P in vivo MRS of liver or muscle and tuned for phosphorus. That means that resonance frequency of the coil matches the one of the nuclear spin. For a single coil acting as transmitter as well as as receiver the intensity of the RF excitation profile (\mathbf{B}_1^-) in space follows the same geometry as the coupling of the excited nucleus' NMR signal back to the coil (\mathbf{B}_1^+). But since this intensity distribution of a 'flat' coil is highly inhomogeneous⁹, there are two different approaches for correction in quantification: the use of an internal reference, i. e. comparison of two peaks within one spectrum for a relative quantification, and the use of an external reference, i. e. comparison of two peaks originating from the same location in space relative to the coil, but one from an in vivo spectrum (from the studied subject) and the other from a reference, e. g. a phantom with known characteristics, for absolute quantification (see subsection 1.4.1). Compared to other RF coils the surface coil is the easiest applicable since its used sensitive volume is not enclosed but on top of it and is limited roughly to the shape of a hemisphere of one coil radius. Despite this decreasing \mathbf{B}_1 field with distance the coil can give rise to sufficient NMR signals in tissues below the surface. The advantage of double tuned coils including an ^1H loop is that these coils support imaging which improves localization for the spectroscopy since it is measured from the same position (same coil). Also \mathbf{B}_0 inhomogeneity is measured with a proton coil and can be corrected for by *shimming*, i. e. changing the main magnetic field due to various coils surrounding the bore of the scanner to reach a relatively homogeneous field distribution [1, 4, 7].

⁹high transmitted signal intensities near to (the center of) the coil, which decrease with increasing distance

Table 1.3: Mean concentrations \pm standard deviations ($^{\text{mmol/L}}$) of some hepatic metabolites of healthy volunteers (A. Laufs et al. (2014) [12] and M. Chmelík et al. (2008) [9]).

	n	[PME]	[P _i]	[PDE]	[γ -ATP]	[α -ATP]
Laufs et al.	85	1.98 \pm 0.58	1.99 \pm 0.51	8.01 \pm 2.17	2.74 \pm 0.55	2.66 \pm 1.19
Chmelík et al.	10	2.24 \pm 0.32	1.37 \pm 0.22	11.40 \pm 3.04	2.14 \pm 0.32	–

1.4.3 ^{31}P MRS in Liver

The liver is well suited for ^{31}P MRS to study bioenergetics since it is a large and relatively homogeneous organ and metabolically very active. Its anatomic position is not too deep inside the body and therefore it can be assessed with a surface coil. Quantifiable metabolites in the liver are PME, P_i, PDE and γ -, α - and β -ATP. Table 1.3 lists measured concentrations of these phosphorus compounds at 3 T. Unlike as mentioned in subsection 1.3.4 PCr is not present in the liver. Its relatively high concentration in muscles, however, can be used to distinguish the origin of localized spectra at the border of these tissues. The PME peak consists of signals from phosphocholine (PC) and phosphoethanolamine (PE) amongst others. Glycerophosphorylcholine (GPC) and glycerophosphorylethanolamine (GPE) give most contribution to the PDE signal. Using higher field strengths than 3 T (e. g. 7 T) it is possible to resolve these and even more compounds like phosphatidylcholine (PtdC), nicotinamide adenine dinucleotide (NADH) and uridine diphosphoglucose (UDPG) [5, 11].

In some hepatic pathologies relative quantification of phosphorus concentrations might not show a difference to healthy livers. This might originate from regulation mechanisms of the liver to adapt the concentration ratio between two metabolites. Although these two metabolites occur in the same quantity relative to each other, their absolute concentrations might have changed much. Therefore absolute quantification provides more detailed information, e. g. to describe liver dysfunctions and metabolites involved in it [5].

1.5 Aims

As mentioned in subsection 1.4.3 ^{31}P MRS is suitable for liver examinations and by means of concentrations of various phosphorus compounds hepatic metabolism can be analyzed on a molecular basis. This noninvasive in vivo examination offers the possibility to get a better understanding of bioenergetics. Comparing metabolic concentrations of healthy people to patients with different liver dysfunctions is a way to study individual hepatic pathologies. The aim of this thesis is *absolute* quantification of phosphorus metabolites which gives insight in liver diseases where relative quantification methods fail.

Based on the study of Chmelík et al. (2008) [9] on a 3 T system the absolute quantification should be performed at a magnetic high field of 7 T: 3D-CSI measurement with an external reference phantom for absolute quantification. The expected advantages of a higher field strength is beyond the higher SNR an increase in spectral resolution and thus quantification of more individual phosphorus compounds which can not be resolved with 3 T. But the high magnetic field bears also challenges, e. g. due to increased \mathbf{B}_1 inhomogeneity. A tool programmed in IDL (Interactive Data Language) (Exelis VIS, Boulder, Colorado, USA) by Marek Chmelík for automated evaluation needed to be adapted. Since the systems' manufacturers were different and therefore the data formats differed the program had to be modulated in many code blocks. A protocol is created and methods are shown for a stable measurement of phosphorus metabolites in the liver in vivo.

Materials & Methods

2.1 Materials & Volunteers

2.1.1 MR Scanner & Surface Coil

All experiments were performed on the 7 T whole-body MRI system MAGNETOM (Siemens Healthcare, Erlangen, Germany; Figure 2.1, left) at the MR Center of Excellence at the General Hospital of Vienna. The use of 7 T instead of 3 T leads to higher SNR as well as an improvement in spectral resolution (see subsection 1.4.3). For the spectroscopy a double-tuned $^1\text{H}/^{31}\text{P}$ surface coil (RAPID Biomedical, Rimpar, Germany; Figure 2.1, right) was used. The coil diameters are 9.5 cm for the ^1H loop and 10.5 cm for the ^{31}P loop. A tuned coil is a coil with its resonance frequency matched to the nucleus under investigation.

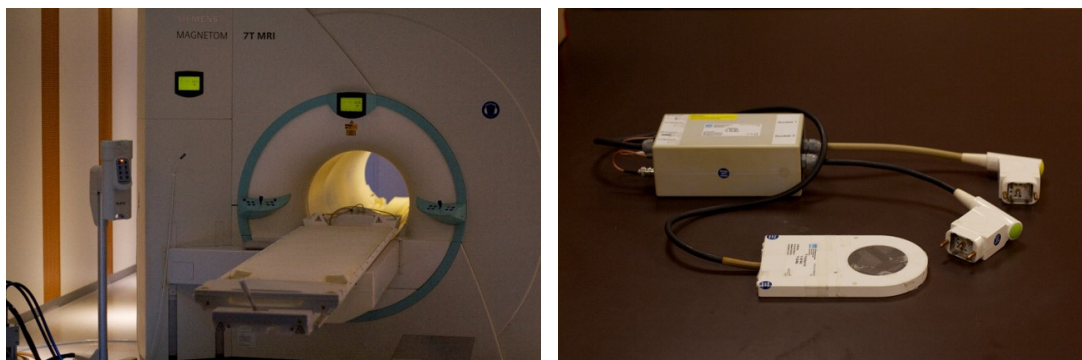


Figure 2.1: Left: 7T scanner MAGNETOM (Siemens Healthcare, Erlangen, Germany); right: $^1\text{H}/^{31}\text{P}$ surface coil (RAPID Biomedical, Rimpar, Germany).

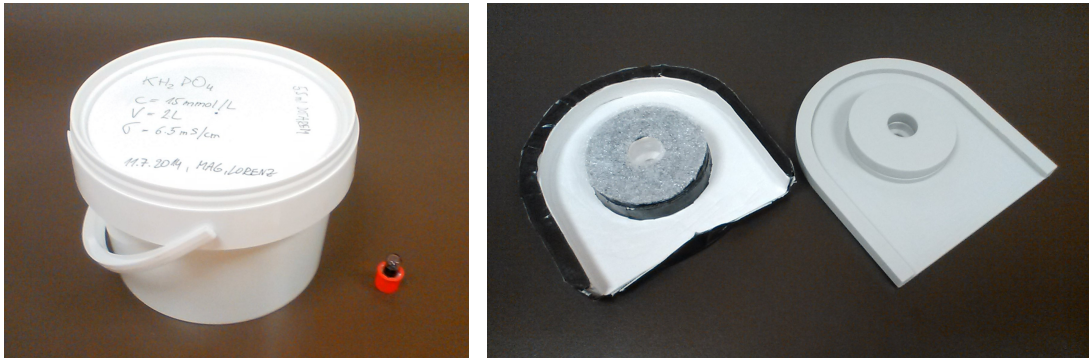


Figure 2.2: Left: big phantom (bucket) and small calibration reference (red cap); right: prototype holder (left) and second generation holder (right).

2.1.2 Phantoms

For the calculation of the absolute concentration in vivo a phantom with known ^{31}P concentration is used. It consists of distilled water added by the right amount of KH_2PO_4 to reach a concentration of 15 mmol/L . It is in a cylindrical bucket with a diameter of 17 cm, height of 9 cm and is 2L in sum (Figure 2.2, left, bucket). To shorten T_1 to a convenient time the phantom is doped with 5.5 mL of gadotric acid (Gd-DOTA, trade name Dotarem). By adding table salt (NaCl) the electrical conductivity can be increased. This phantom was adjusted to a conductivity of 6.5 mS/cm . The reason behind is to simulate physiological conditions as well as possible, specifically in matters of phosphorus concentration and electrical conductivity. Adding up the measured concentrations of Table 1.3 results in $15\text{--}20 \text{ mmol/L}$ so a phantom with a concentration of 15 mmol/L should meet the requirements. For a magnetic field strength of 7 T the resonance frequency of ^{31}P is at about 120 MHz (see Table 1.1). For this frequency the liver shows an electrical conductivity of 5.05 mS/cm and muscle tissue, which is between the liver and the coil, shows one of 7.16 mS/cm [13]. With 6.5 mS/cm the prepared phantom's conductivity is between that of the named tissues.

As purpose of validation, a second phantom (2L) was mixed in a bucket with the same dimensions. Its ^{31}P concentration was adjusted to 25 mmol/L analogous to the other one by adding KH_2PO_4 to distilled water. To shorten T_1 the phantom was doped with 4 mL Dotarem. The electrical conductivity is in accordance with the other phantom with 6.5 mS/cm .

For coil load correction (see subsection 1.4.1) a calibration reference is needed. It is a glass phial with a plastic cap in cylindrical shape (diameter: 10 mm, height: 13 mm). Its volume is 1 mL and contains triphenylphosphate (TPP) diluted in chloroform (Figure 2.2, left, small sample with red cap). To keep it in the same position in space relative to the coil a holder was built. Figure 2.2, right image shows the prototype holder (left), which was made from air-hardening modelling material, reinforced with duct tape and attached by foam material for a soft support, and a second generation holder (right), which was milled from plastics. Both holders offer a tight fit for the coil and the calibration reference in the center.

2.1.3 Volunteers

The participating volunteers were five males at the age of (27 ± 1.8) years and with a weight of (70.2 ± 4.8) kg. To test the necessity of the holder three measurements with different volunteers were performed respectively with and without holder. For repeatability testing each experiment was performed twice successively. The study protocol was approved by the local ethics committee and written, informed consent was obtained from each volunteer.

2.2 Methods

2.2.1 Experimental Setups

As explained in subsection 1.4.1 both in vivo and phantom acquisition need to be performed both in the same way. This was achieved similar to Chmelík et al. (2008) [9] with the exception that the volunteers were not in the prone position but laying head first on the right side lateral on the scanner table (Figure 2.3, B). The surface coil and the calibration reference were both mounted on the holder to stay in fixed position to each other. The liver needs to be directly above the coil. Therefore, controlled by a ^1H MR localizer scout image obtained by the proton channel of the surface coil small corrections were performed. For the phantom measurement, the bucket was placed central on top of the coil-holder combination (Figure 2.3, A).

Both acquisitions were performed with equivalent scanner settings. Thus the FOV was set to $20 \times 20 \times 20 \text{ cm}^3$ with the calibration reference always at the same location in it. As a next step shimming (see subsection 1.4.2) was performed to a prescribed adjustment volume positioned within a homogeneous part of the VOI. Therefore, a signal was acquired on the proton channel of the coil and a provided automatic procedure and further manual adaptation was used for adjustments. This volume should be homogeneous and centered to the coil and it should neither reach too close to the surface nor too deep into the subject (to get sufficient not contaminated signal) (Figure 2.4). After these preparations a nonlocalized spectroscopic test sequence was run. When showing sufficient signal and acceptable spectral resolution the 3D-CSI sequence was started. Subsequently a multi-slice localizer with same FOV and orientation was acquired in order to allocate the 3D-CSI grid to the anatomical images. Further details about the used sequences are explained in the next subsection 2.2.2.

2.2.2 MR Protocols

T_1 Determination of the Phantoms

Inversion recovery pulse sequence was performed for assessment of T_1 relaxation times of phantom solutions. Two measurement series were acquired for evaluating signal amplitudes. A fast one with 10 different T_I times between 20 and 15,000 ms¹ and a more precise one with 18 different T_I times between 20 and 20,000 ms². T_R was set to 40 s for both series. The longer one or the combination of both series is used to compute T_1 due to graph fitting according to the following formula [8]:

$$I = I_0 \left(1 - 2 e^{-T_I/T_1} \right) \quad (2.1)$$

where I_0 is the initial signal integral and I the signal integral after inversion and passing the time T_I . The missing parameters I_0 and T_1 are then determined and a correlation coefficient of the regression curve indicates how reliable these values are. T_1 of the phantom was adjusted by iterative doping with small doses of Dotarem.

¹20, 350, 1200, 1700, 2300, 2700, 3300, 3700, 4500 and 15000 ms

²20, 25, 50, 100, 150, 300, 400, 500, 600, 700, 850, 1000, 1500, 2000, 3000, 5000, 10000 and 20000 ms

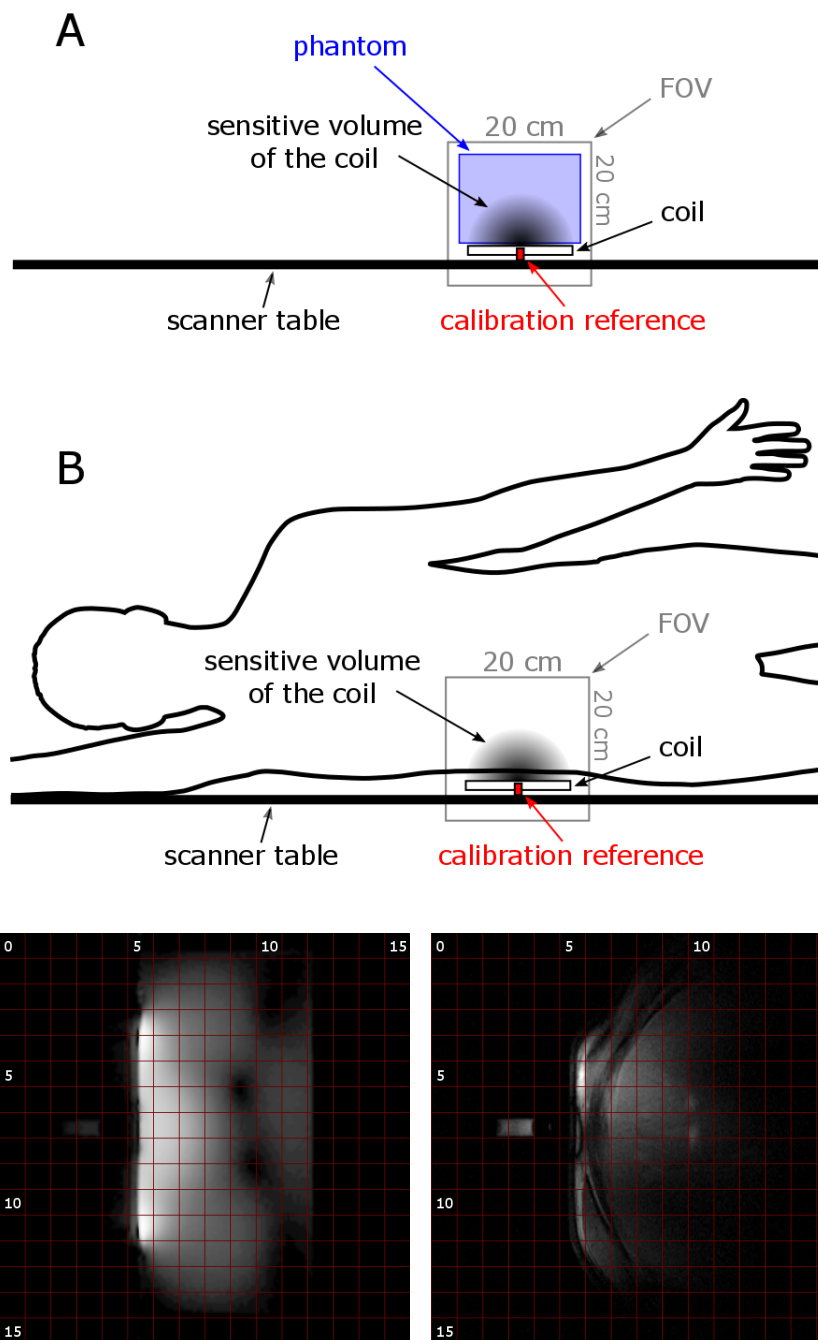


Figure 2.3: Top: phantom (A) and in vivo (B) positioning; bottom: the corresponding phantom (left) and in vivo (right) localizer images of the FOV with 3D-CSI grid rotated 90° clockwise.

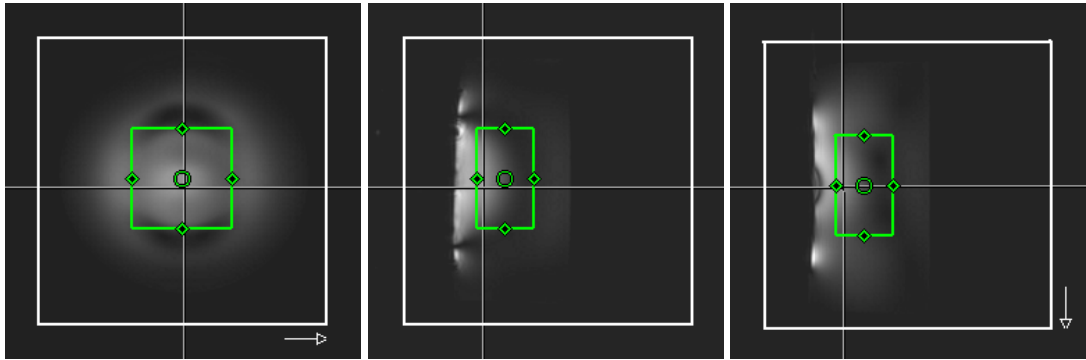


Figure 2.4: Three localizer views of a phantom scan perpendicular to each other: gray squares indicate FOV and green rectangles define the adjustment volume for shimming.

Pulse Adjustment

Three different excitation pulses were tested in order to achieve optimal B_1 strength and homogeneity: adiabatic half-passage with a pulse length of $2,500\ \mu\text{s}$ (AHP2500) and one with a pulse length of $3,000\ \mu\text{s}$ (AHP3000) and a rectangular pulse with length of $600\ \mu\text{s}$ (RECT600). For each sequence a series with different pulse amplitudes was acquired: The amplitude of AHP pulses was tested in the range of 50 to 250 V with increments of 20 V, for the RECT600 the range was 100 to 300 V with increments of 20 V. For every single measurement T_R was specified to 20 s. The experimental setup was equivalent to the actual 3D-CSI measurement. So a volunteer was lying with head first on the right side lateral on the scanner table with the liver placed directly above of the coil. After shimming the nonlocal sequences AHP2500, AHP3000 and RECT600 were measured with different voltages as described above. The three acquired spectra series were then compared and due to the voltage dependent trend of the metabolites' peaks the most suitable excitation pulse was chosen.

The main sequence for absolute quantification is ^{31}P 3D-CSI. The spectra were acquired by k-space weighted localization using 12 phase-encoding gradients in all three directions. As excitation pulse RECT600 was used and T_R was set to 1.8 s. By postprocessing with spatial zero-filling the data were extended to a $16 \times 16 \times 16$ matrix of the same FOV of $20 \times 20 \times 20\ \text{cm}^3$. The FIDs were recorded with a spectral width of 5,000 Hz and 1024 complex points. To make the dependency of the penetration depth on the pulse amplitude visible the following experiment was performed: A series of 3D-CSI measurements of one phantom was acquired with varying reference voltages from 50 V to 300 V increasing successive by 10 V. The phosphorus signals were integrated and the resulting values were mapped by color on the $16 \times 16 \times 16$ grid. From this experiment it was deduced which pulse amplitude is most practical for phantom measurements. For verification reasons of the spatial signal distribution a simulation was performed. The calibration reference, the surface coil and their orientation in the simulation were adapted to be as accurate to the real experiment as possible. An average human model was chosen. Transmitted signal intensity and received sensitivity distribution were then computed using body model, as well as of a model including the liver only.

Due to the nonuniform excitation pulse profile phantom 3D-CSI measurements were performed with different frequency offsets to provide the right correction matrices for the single metabolites for absolute quantification: 915 Hz (α -ATP), 300 Hz (γ -ATP), 0 Hz (PCr), -385 Hz (PDE), -615 Hz (P_i) and -800 Hz (PME)³. Out of previous measurements with a 50 mmol/L phantom at the listed offset frequencies correction factors were computed in order to compensate for the nonuniform excitation pulse profile. For the calculation of these correction factors different methods were compared: One was to use the maximum value of each 3D-CSI data set with offset and divide it by the maximum one at zero offset. The other method used a cuboid of representative voxels reaching from 7 to 9 in x -direction, from 4 to 7 in y -direction and from 6 to 9 in z -direction. (The whole 3D-CSI voxel grid reaches from 0 to 15 in each direction.) Each voxel of that volume from each 3D-CSI data set with offset was then divided by the corresponding one at zero offset. Out of these gained voxel dependent correction factors a mean value was calculated for each 3D-CSI data set for a total correction according to its frequency offset.

Positioning of the calibration Reference

Subsequently to the 3D-CSI a gradient-echo localizer sequence of the same size ($20 \times 20 \text{ cm}^2$) and orientation was acquired for allocating voxel slices to images in axial planes. Therefore 12 axial slices with 12 mm thickness and matrix sizes of 320×320 are acquired. These are then interpolated to 16 images in order to match the number of voxel slices in axial direction. T_R was specified to 7.4 ms and T_E to 3.43 ms.

Because of variations in the signal integral of the calibration reference in equivalent experiments (successive measurements with complete repositioning) the question arose whether different positions relative to the coil could explain this. Therefore a series of measurements with non-localized sequences was recorded where the calibration reference was placed in various depths and its signals were integrated and the results were plotted against position values. These values are the distances of the upper surface of the calibration reference to the bottom of the phantom measured by means of localizer images described above with syngo fastView (Siemens Healthcare, Erlangen, Germany).

Another experiment was performed to compare directly the influence of the holder. Successive measurement data with and without holder were recorded both with phantom as well as in vivo. After each measurement the subject, the coil and the calibration reference were repositioned. Then the signal integrals of the calibration reference were compared. The use of the holder lead to splitting up of the resonance peak into two peaks. This issue was investigated by visualizing B_0 inhomogeneity with field maps using MATLAB (MathWorks, Natick, Massachusetts, USA). The field maps were calculated out of the difference of two gradient-echo images acquired with different T_E times. Furthermore it was attempted to prevent the peak splitting with dielectric pads placed around the coil-holder combination.

³listed metabolites in brackets give rise to peaks around the corresponding frequency at 7 T

Phantom Testing

For validating the absolute quantification method 3D-CSI data of one phantom are compared to that of another phantom. Both phantoms have known phosphorus concentration and one is used for correction in the same way as for in vivo data. If the method works suitable, the result should be equal or close to the known concentration of the second phantom. In early measurements a phantom with 50 mmol/L was used for correction and two phantoms with 100 mmol/L and 150 mmol/L were mixed for validation. Due to several problems all of these phantoms were rejected and two new ones were made as described in subsection 2.1.2. The validation experiment was performed with these new, more physiological phantoms in the same way as in vivo absolute quantification (see next subsection 2.2.3). 100 voxels were chosen for quantification. The results are stated in subsection 3.2.1.

2.2.3 Workflow & Postprocessing

After acquiring the in vivo 3D-CSI data it is visualized in an IDL tool created in-house by Marek Chmelfik and adapted for processing data from the 7 T Siemens scanner (Figure 2.5). The tool is able to plot the real and imaginary part as well as the absolute values of the spectrum from each voxel (Figure 2.5, top left plot). The voxels are chosen from a grid for each slice in axial direction which can be overlaid with localizer images covering the same FOV for better allocation (Figure 2.5, bottom right plot). Multiple voxels can be selected and a sum of their spectra can be plotted (Figure 2.5, bottom left plot). The tool is also able to phase spectra, filter them by line broadening and perform zero-filling. Another very important feature is the Hamming filter which can be applied half (50 %) or complete (100 %). The first step for absolute quantification is determining the calibration reference's peak height to scale spectra and correct for different coil loads. Therefore, the spectra from a volume of $5 \times 5 \times 5$ voxels around the voxel with maximum signal integral (originating from the calibration reference) in the center were summed up and exported. Now a VOI of voxels within the liver was chosen for quantification according to following conditions: The voxels need to be located in the liver by means of the localizer images. Only voxels with signal without PCr (skeletal muscle exclusion) and with sufficient SNR (with at least one peak above 2) were included. The signals from the selected voxels were exported for further processing.

The peak quantification was performed with jMRUI (Java-based magnetic resonance user interface) [14] software using AMARES (advanced method for accurate, robust, and efficient spectral fitting of MRS data with use of prior knowledge) [15]. First the peaks of the signal sum of the calibration reference need to be fitted. This was achieved with the following prior knowledge in AMARES: Three Lorentzian shaped curves with soft constraints in frequencies, phases and line widths were used. For two of these the frequency range was set around one peak and for the third it was set around the other peak. The phases were restricted within $\pm 90^\circ$ and the line widths were limited to 300 Hz. The overall phasing was fixed since the summed spectrum was exported in absolute values. The weighting was activated with the first five points. The results were saved for later re-importation to the IDL tool.

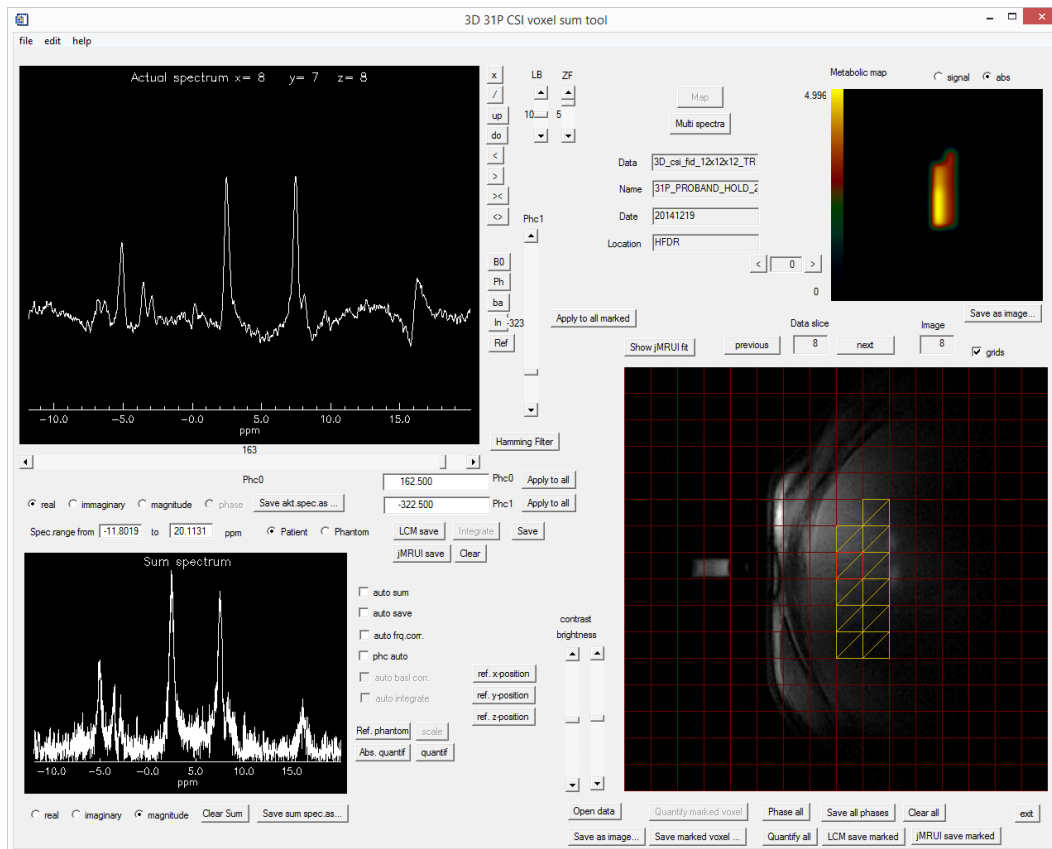


Figure 2.5: Screenshot of the IDL tool.

As a next step the exported voxels from the VOI were quantified. Therefore, the single spectra were individually phased in jMRUI and fitted with the following prior knowledge in AMARES: All available phosphorus metabolite signals⁴ were fitted with Lorentzian functions. Except for the ATP signals for all other metabolites one line with soft constraints in frequency range around its maximum and line width restriction from 1 to 50 Hz was used. Both γ - and α -ATP were fitted with two lines with estimated but equal amplitude, phase and line width and with soft constraints in frequency for one peak and 16 Hz distance to that for the other. For β -ATP three Lorentzian functions with no restrictive parameters were used for quantification⁵. Together with the jMRUI results of the calibration reference, the metabolite results were re-imported into the IDL tool. Now the absolute quantification can be performed: The software loads prior quantified phantom data and T_1 times of Table 1.2 so that all necessary parameters of equation (1.55) are available. The concentration of the different metabolites for each voxel of the VOI is calculated according to that formula. A metabolic map displays the quantified concentration distribution of each metabolite in each slice in axial direction (Figure 2.5, top right).

⁴ γ -, α -, β -ATP, PCr, GPC, GPE, P_i, PC, PE, UDPG, NADH and PtdC

⁵doublets and triplets appear due to so called spin-spin coupling

As mentioned earlier the tool is able to apply a Hamming filter on the data in the k-space. For the presented data in chapter 3 all 3D-CSI measurements were evaluated with a full Hamming filter of 100 %. Thereby, the advantage is the suppression of voxel bleeding which contaminated signals in voxels located in the liver with PCr signals originating from the muscles. So the number of voxels which fulfill the conditions for absolute quantification (stated earlier in this subsection) can be increased.

2.2.4 IDL Tool Adaptions

As already mentioned the used IDL tool by Marek Chmelík had to be adapted in many code blocks. First of all the recorded 3D-CSI data were in different data formats and therefore, the data loading block had to be rewritten including all the parameter loading from the header. The same was valid for the image loading. Since the patient positioning was different as well, the data and images had to be rotated to display it for better orientation. The application of a Hamming filter (50 & 100 %) was implemented as optional choice by extracting and testing it from comparing filtered and unfiltered data sets. To check the quality of the quantification of a spectrum a button was added on which the corresponding jMRUI fitting image of that voxel was displayed containing the original spectrum, the individual fitted peaks and the sum of these as well as the residual spectrum. Maps (with 0, 50 and 100 % Hamming filter) containing the signal integrals of the correction phantom were created and automatically loaded by the IDL tool on selecting absolute quantification. The factors needed for saturation correction were not directly defined in the tool but calculated from the T_1 times of a table of a predefined external file. Due to higher spectral resolution more single metabolites could be detected and the whole code blocks for quantification and presenting the results needed to be extended and adapted to process the spectra correctly. For correcting for the nonuniform excitation pulse profile the corresponding factors were defined in the tool and applied on the different metabolite signals.

3.1 Preparations

3.1.1 T_1 Determination

As described in subsections 2.2.2 T_1 of the phantoms had to be determined. Integration of the measured signal peaks and graph fitting according to equation 2.1 lead to a T_1 time of 1,362.00 ms with a coefficient of determination of 0.9993 for the 15 mmol/L phantom used for saturation correction in the IDL tool. The 25 mmol/L validation phantom reached a T_1 of 1,844.00 ms with a coefficient of determination of 0.9991.

3.1.2 Pulse Adjustment

The AHP2500 and AHP3000 sequences showed similar results for pulse adjustment: The PCr signal rose with increasing voltage until it reached a limit and then stagnated within a certain range (Figure 3.1, right). Signals from other metabolites showed no specific behavior. In contrast to that the RECT600 pulse sequence suppressed the PCr signal more and more with increasing voltage while other signals stay unaffected (Figure 3.1, left). Figure 3.2 shows the parameter evolution of signal integrals of the used pulses. Negative values indicate that the phase for quantification changed more than $\pm 90^\circ$ from the initial spectrum. With a reference voltage above 200 V the PCr signal suppression is very strong.

The dependence of penetration depth on the used excitation pulse with different reference voltages is visualized in Figure 3.3. The figure shows that with higher pulse amplitudes the penetration into the phantom is deeper, but the maximum signal reduces and a half sphere with very little signal spreads into the phantom and causes additional inhomogeneity. Simulated data (Figure 3.4) show that the signal distribution in the human body is similar to the one measured in the phantom with the same sequence.

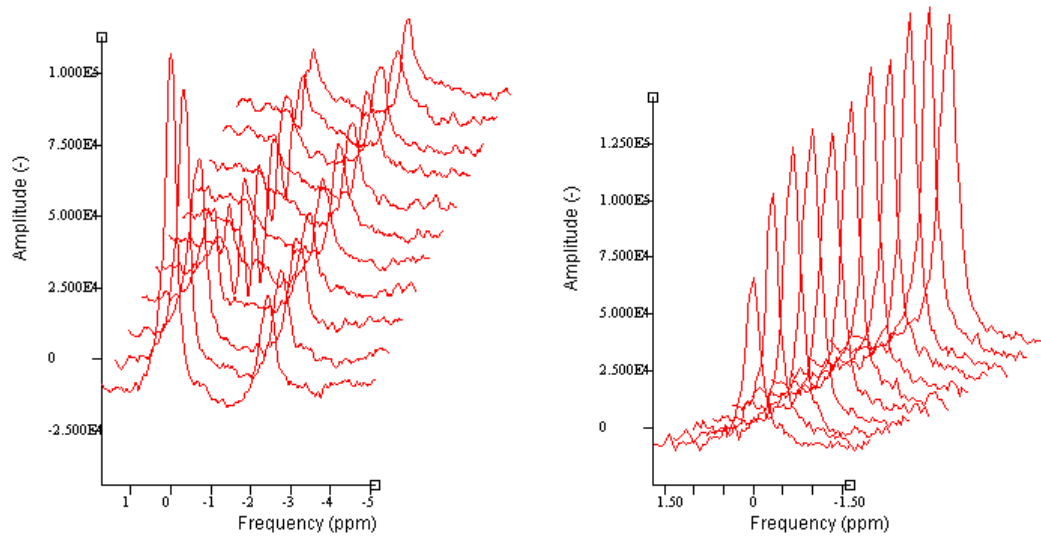


Figure 3.1: Left: PCr (left peak) and γ -ATP signal (right peak) with RECT600 sequence at different voltages (see subsection 2.2.2 Pulse Adjustment); right: PCr signal with AHP3000 sequence.

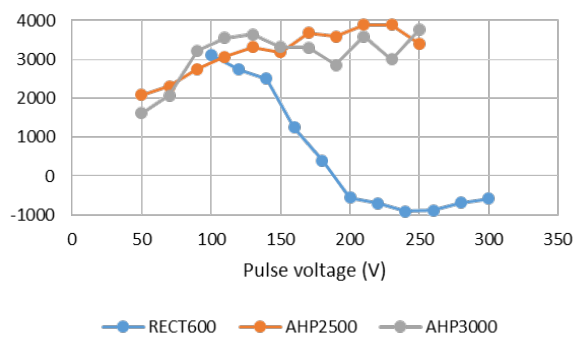


Figure 3.2: PCr signal integral evolution of the different sequences used.

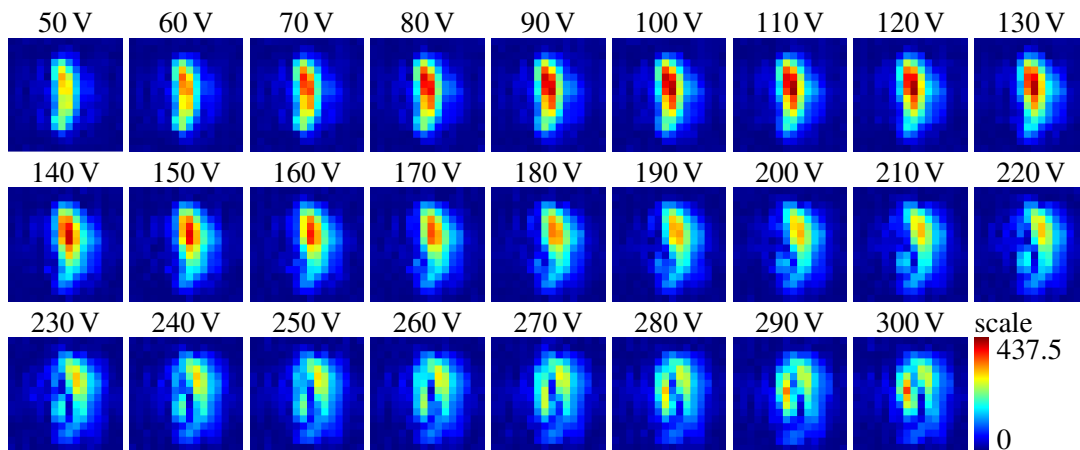


Figure 3.3: ^{31}P 3D-CSI signal integrals of the phantom with increasing reference voltage (see subsection 2.2.2 Pulse Adjustment) scaled to the maximum over all at a slice in the middle (slice 8 of slices 0-15).

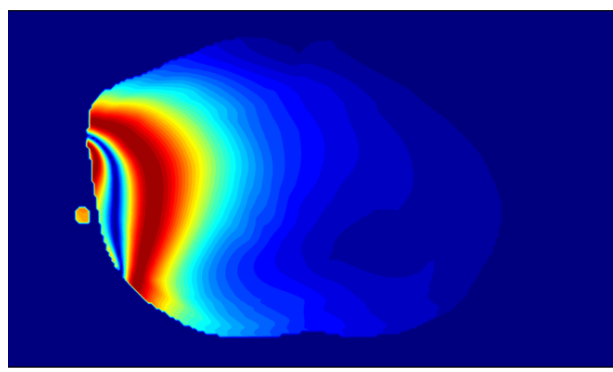


Figure 3.4: Simulation of transmitted signal intensity in the human body (transversal plane through the body at the liver, small sphere on the left symbolizes calibration reference).

The calculated correction factors for the nonuniform pulse profile of the two different approaches explained in subsection 2.2.2 Pulse Adjustment are depicted in Figure 3.5. The problem about taking the maximum values of the signal integrals of each 3D-CSI grid for correction is that their position varied. So the correction factors were calculated out of a cuboid of representative voxels. The error bars refer to as the standard deviation of the voxel dependent correction.

3.1.3 Positioning of the Calibration Reference

Varying the distance of the calibration reference to the phantom means also changing it respectively towards the surface coil since the phantom is placed directly on top of the coil. Figure 3.6 shows the signal integrals resulting from different distances and a linear regression curve calculated from those. The linear regression function has a slope of -78.07 and a y-intercept of

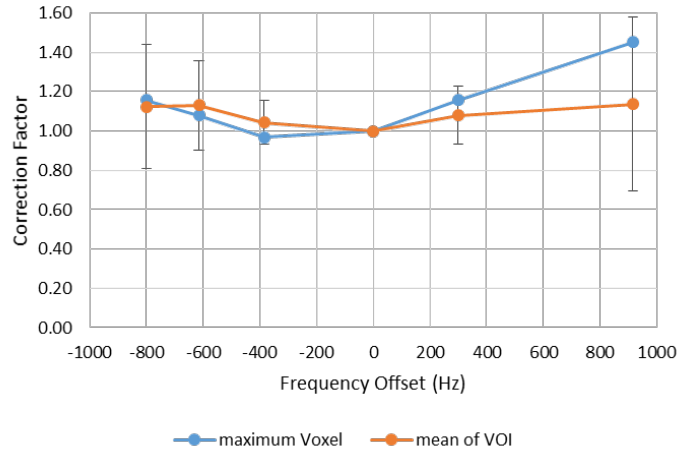


Figure 3.5: Correction factors calculated with different approaches.

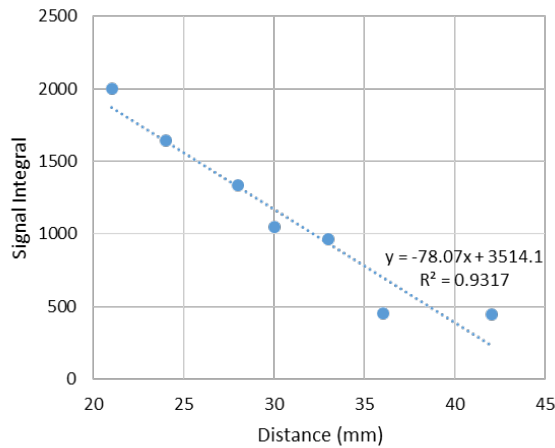


Figure 3.6: Signal integrals of the calibration reference at different distances from the phantom and its linear regression (dotted line).

3,514 with a coefficient of determination of 0.9317. Considering this being the actual trend line a variation of ± 1 mm means a deviation of around 78. So at a distance of 20 mm with a signal integral slightly below 2,000 an offset of ± 1 mm results in about 4 % deviation.

For testing the stability of the calibration reference's signal integral several 3D-CSI measurements with and without holder were performed. In total 7 measurements with the phantom (15 mmol/L) with equal conditions without holder were available where two times 2 were recorded successively. The mean value of the signal integrals was 2,729.58 with a standard deviation

Table 3.1: Comparison of the signal integral of calibration reference with and without holder (ph. xx ^{mmol/L}: phantom with xx ^{mmol/L} ³¹P, stdev. abs./rel.: absolute/relative standard deviation, dist.: distance of calibration reference to subject (mean ± standard deviation)).

subject	holder	n	mean	stdev. abs. / rel. [%]	dist. [mm]	
ph. 15 ^{mmol/L}	none	7	2,729.58	285.33	10.45	36.3 ± 0.76
ph. 15 ^{mmol/L}	prototype	3	6,847.14	433.08	6.32	26
ph. 15 ^{mmol/L}	2nd gen.	5	24,114.20	911.62	3.78	19
ph. 15 ^{mmol/L}	none	1	31,354.00	–	–	20
ph. 25 ^{mmol/L}	none	4	4,498.58	709.95	15.78	35.0 ± 1.63
ph. 25 ^{mmol/L}	prototype	3	7,482.00	267.79	3.58	26
ph. 25 ^{mmol/L}	2nd gen.	1	26,998.30	–	–	19
in vivo #1	2nd gen.	2	24,295.55	1,581.44	6.51	17
in vivo #2	2nd gen.	2	40,594.65	3,438.17	8.47	17
in vivo #3	2nd gen.	2	38,381.65	606.63	1.58	17
in vivo #4	none	2	8,767.45	4,145.70	47.29	32.5 ± 0.71
in vivo #5	none	2	6,914.40	4,024.14	58.20	29.5 ± 0.71
in vivo #6	none	2	9,797.05	254.49	2.60	32.0 ± 0.00

of 258.33 (10.45 %). The measured distances from the calibration reference to the phantom by means of localizer images were between 35 and 37 mm (36.29 mm ± 0.76 mm)¹. The same experiment was performed with the holder (2nd generation) 5 times with 3 and 2 times successively. This resulted in a mean signal integral of 24,114.20 with a standard deviation of 911.62 (3.78 %). The measured distance of the calibration reference was fixed at 19 mm. A summary of experiments performed to evaluate the necessity of the holder is listed in Table 3.1. The use of the holder lead to a splitting up of the resonance peak in to two peaks (Figure 3.7). It was also checked whether the two peaks amount to the same signal integral than one resonance without holder with the calibration reference at the same distance as with holder². The result of 31,354.00 shows that there is quite some difference compared to 24,114.20 (mean of 5 measurements). In addition 6 in vivo experiments were performed whereof 3 with holder and 3 without. Each contained 2 successive measurements. The ones with holder had relative standard deviations below 10 % whereas the others relative standard deviation were around 50 % and even higher with one exception of 2.6 % by chance.

The splitting up of the resonance peak was investigated with field mapping. Figure 3.8 shows the **B₀** field map of the calibration reference and surrounding without (left) and with holder (right). The red rectangular marks the calibration reference. On the right image borders a part of the phantom is visible. While **B₀** seems quite homogeneous without holder with holder there are some strips indicating phase wrappings. Attempts to prevent these field inhomogeneity by the use of dielectric pads placed beyond the holder partly around the calibration reference did not lead to the desired result. There was hardly a difference detectable.

¹mean ± standard deviation

²actual distance measured reached 20 mm

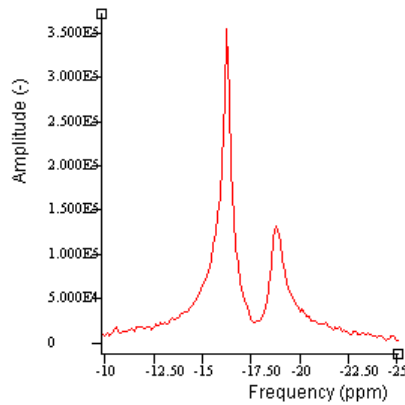


Figure 3.7: Splitting of the resonance peak of the calibration reference.

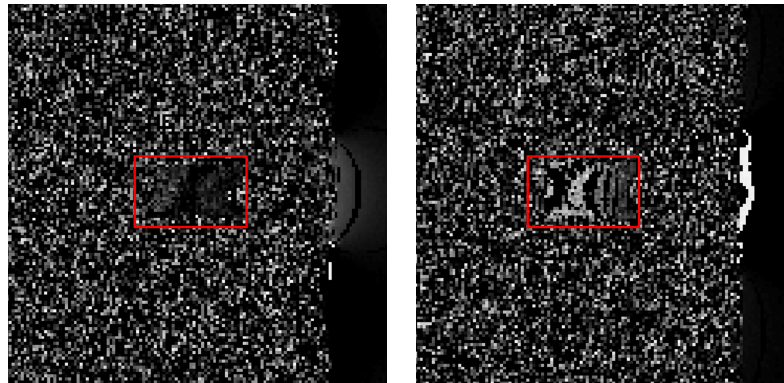


Figure 3.8: Field maps of the calibration reference (red rectangular) and surroundings without (left) and with holder (right). On the right image borders the phantom is visible.

3.2 Absolute Quantification

3.2.1 Phantom Validation

In the same way as described in subsection 2.2.3 the validation phantom (25 mmol/L) is processed against the data of the correction phantom (15 mmol/L). A middle slice of the signal integral maps of both phantoms is depicted in Figure 3.9. The validation was performed with 100 voxels. Figure 3.10 shows some selected voxels (left) and the computed signal integrals and metabolic maps (right) of the same slice. The top two images on the right depict quantification without the application of a Hamming filter where the left one visualizes the jMRUI results and the right one the absolute quantification scaled to the maximum of 31.60 mmol/L . Analogously, the quantification with 100 % Hamming filter is shown in the bottom two images on the right with the signal integrals (left) and the metabolic map scaled to the maximum of 25.37 mmol/L (right). Without the use of a Hamming filter the mean value of the 100 quantified voxels resulted in

a ^{31}P concentration of 26.12 mmol/L with a standard deviation of 4.11 mmol/L . When applying the full Hamming filter the absolute quantification lead to an underestimation of the phosphorus concentration with a mean value of 21.86 mmol/L and a standard deviation of 2.13 mmol/L .

3.2.2 Hamming Filter

Figure 3.11 depicts the effect of the Hamming filter to an in vivo measurement by means of the calibration reference. The calibration reference is chosen for demonstration since its actual size is small but it has a high concentration of phosphorus. The metabolic map visualizes how the PSF influences the measured signal. The right image shows the signal developing along a line through the calibration reference (black column of left image) and how it is changed by the use of different strong Hamming filters: With stronger filtering the side lobes and also the signal maximum decrease but the FWHM increases slightly.

The effect of the Hamming filter on single spectra can be seen by comparing two spectra of the same voxel and measurement with (100 %) and without it (Figure 3.12). The use of the Hamming filter reduces the signal height of all peaks including noise and therefore improves SNR. At 0 ppm the unfiltered spectrum shows a peak which is strongly suppressed by the application of a Hamming filter. Other peaks do not manifest much variation of their height relative to one other.

3.2.3 Quantification Results in Vivo

The volunteers were measured twice successively with repositioning. Three of the measurement series were performed with and three without holder. For all 12 single measurements a different VOI of voxels fulfilling the desired conditions about very low PCr signal and acceptable SNR were chosen (e. g. Figure 3.13). Figure 3.14 shows one example in vivo spectrum of a voxel in the liver and its fitted peaks in jMRUI using AMARES as well as the residual spectrum.

For each of the single measurements and each metabolite a weighted mean based on signal intensity was calculated from the quantified voxels. The mean values and standard deviations of the results with the use of holder are listed in Table 3.2. The number of selected voxels was between 27 and 72 with a mean of 55.

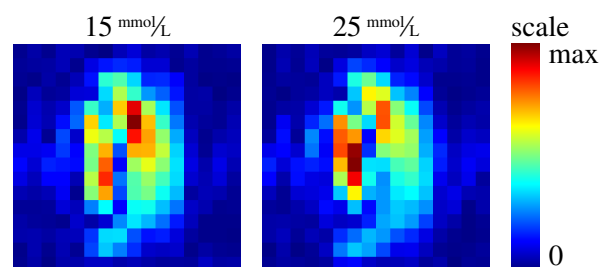


Figure 3.9: ^{31}P 3D-CSI signal integrals of phantoms with different concentrations scaled to the maximum of each map at a slice in the middle (slice 8 of slices 0-15).

³no saturation correction due to missing T_1 of these metabolites at 7 T

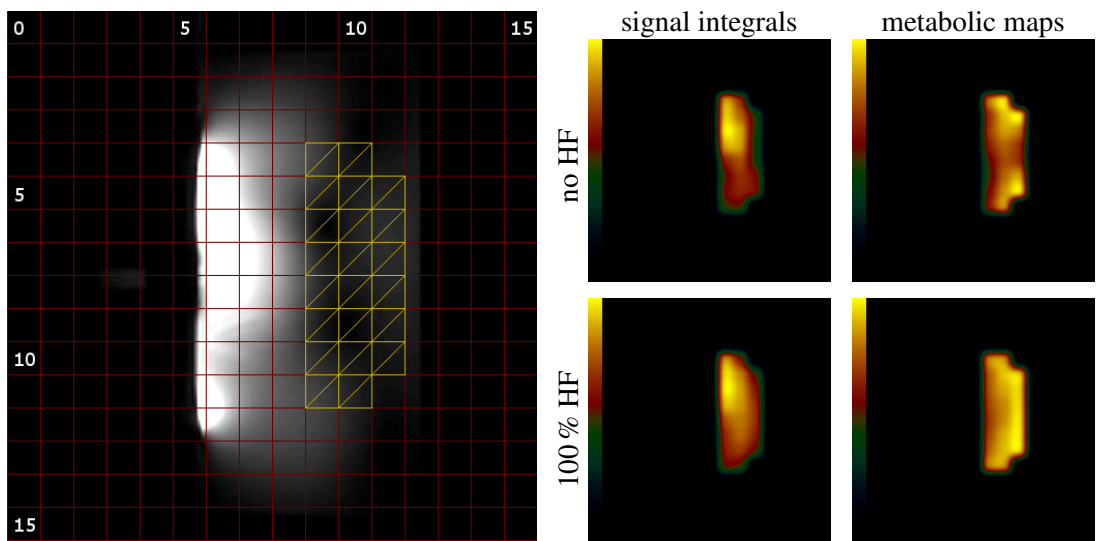


Figure 3.10: Middle slice of validation phantom with selected voxels for quantification; left: selected voxels; top right: quantified signal (left, maximum 257.8) and absolute concentration (right, maximum 31.60 mmol/L) without Hamming filter (no HF); bottom right: quantified signal (left, maximum 184.7) and absolute concentration (right, maximum 25.37 mmol/L) with 100 % Hamming filter (100 % HF).

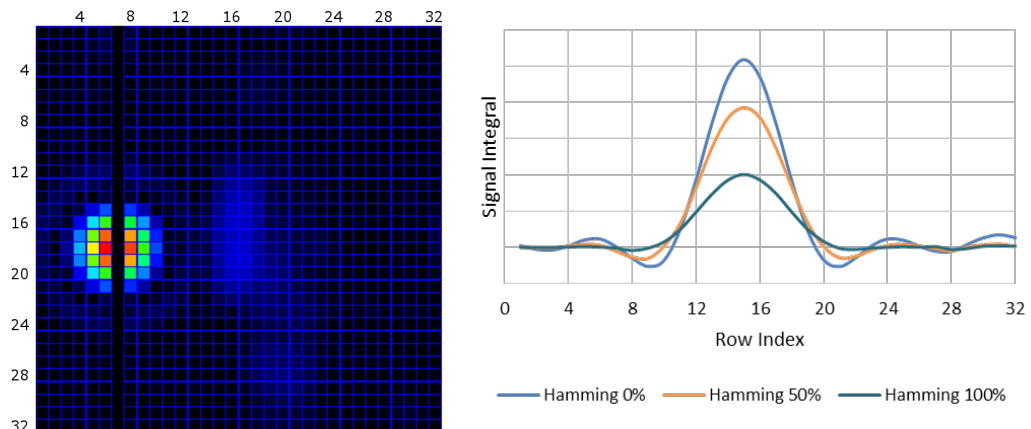


Figure 3.11: Left: Middle slice of metabolic map of calibration reference, interpolated to 32×32 ; right: signal integral of a column through the calibration reference (black column of left image) with application of 0, 50 and 100 % Hamming filter.

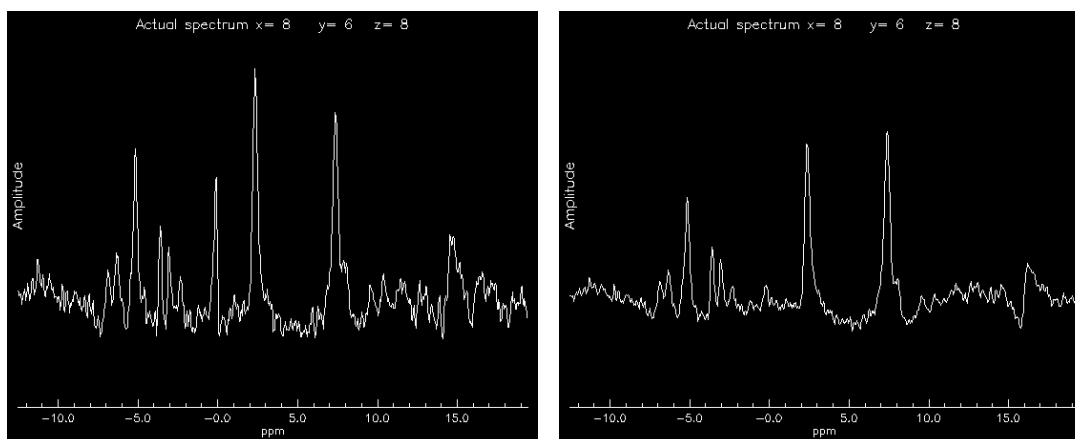


Figure 3.12: Two spectra of the same measurement originating from the same voxel located in the liver; left: without Hamming filter; right: 100 % Hamming filter.

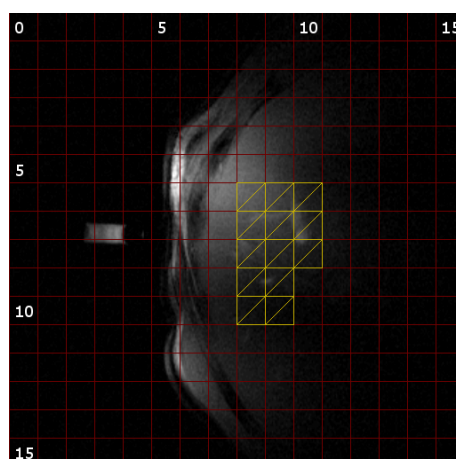


Figure 3.13: Voxels of a middle slice selected for in vivo quantification.

Table 3.2: Calculated mean concentrations and standard deviations (SD) in mmol/L of 3 volunteers with each 2 successive measurements.

	γ -ATP	α -ATP	GPC	GPE	PtdC	P_i	PC	PE	UDPG	NADH
mean	2.68	2.74	3.28	3.61	0.28^3	1.62	1.32	1.23	0.20^3	0.27^3
SD	0.56	0.55	0.84	0.77	0.11^3	0.42	0.38	0.48	0.08^3	0.10^3

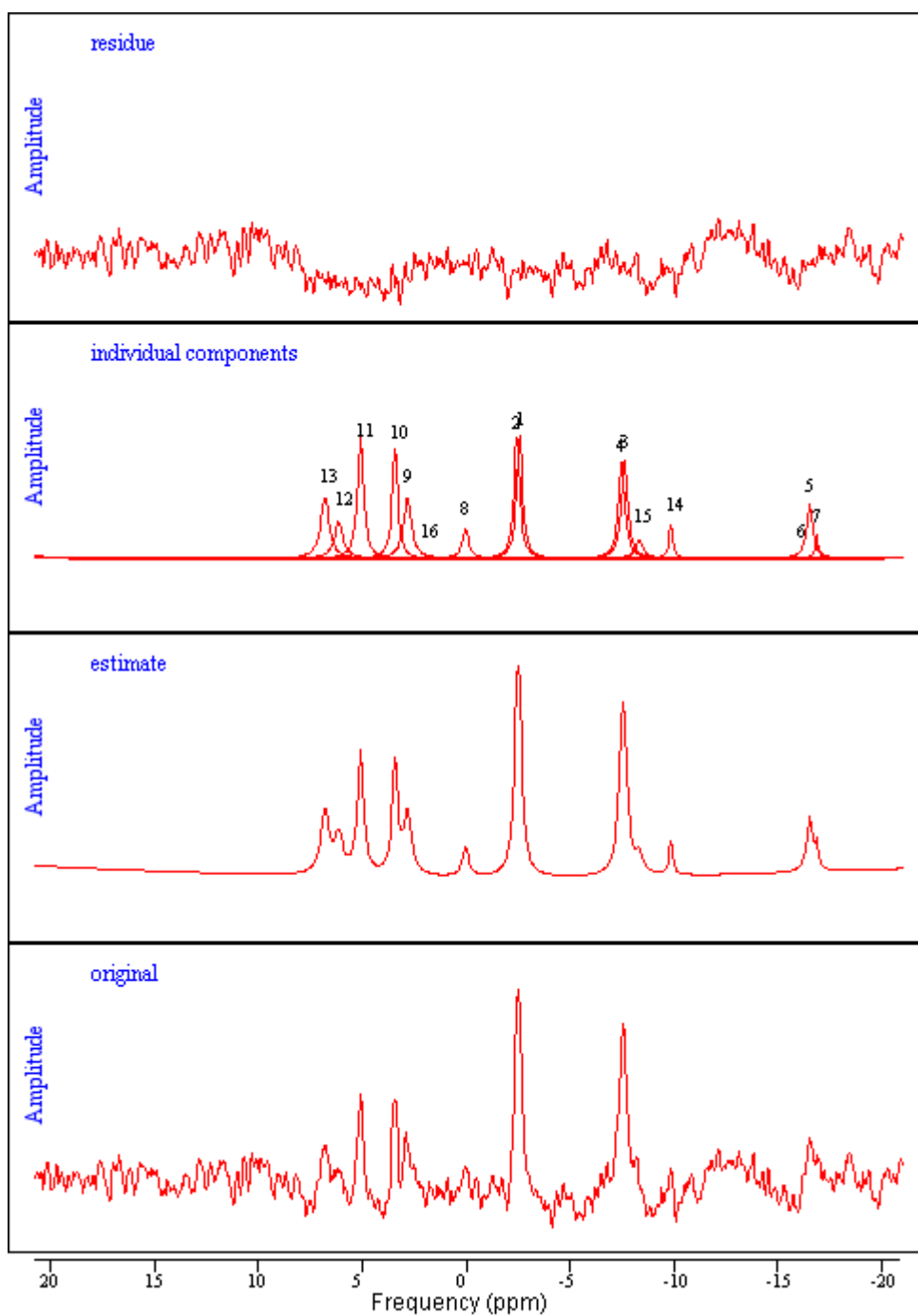


Figure 3.14: In vivo spectrum of a voxel in the liver ($x = 9$, $y = 10$, $z = 6$), estimated fit and its single peaks using jMRUI with AMARES (peaks: 1+2: γ -ATP, 3+4: α -ATP, 5-7: β -ATP, 8: PCr, 9: GPC, 10: GPE, 11: P_i , 12: PC, 13: PE, 14: UDPG, 15: NADH, 16: PtdC) and residual spectrum.

Table 3.3: Calculated mean concentrations and standard deviations (SD) in mmol/L of 3 volunteers with each 2 successive measurements without the use of a holder and without Hamming filter.

	γ -ATP	α -ATP	GPC	GPE	PtdC	P_i	PC	PE	UDPG	NADH
mean	1.16	1.31	1.17	1.57	0.17 ³	0.67	0.58	0.42	0.11 ³	0.20 ³
abs. SD	0.55	0.63	0.49	0.87	0.13 ³	0.29	0.33	0.18	0.08 ³	0.11 ³
rel. SD	48 %	48 %	42 %	55 %	74 %	43 %	56 %	42 %	74 %	54 %

Since the experiments without holder showed already huge differences comparing the calibration reference (Table 3.1, in vivo #4 and #5) the absolute quantification varied strongly. The distance of the calibration reference to the subject was also in all in vivo measurements without the use of a holder around 5 mm different from the phantom measurements (Table 3.1) leading to a probable underestimation of all concentrations (Table 3.3). The number of selected voxels was only between 18 and 32.

Discussion

4.1 Preparations

4.1.1 T_1 Determination

The T_1 determinations of the phantoms were stable experiments. Multiple measurements and evaluations¹ showed the same results (within ± 0.01 s). In contrast to that the T_1 times of the metabolites showed quite some variations (Table 1.2). The relative standard deviations of the T_1 times of PE and PC is around 35 %, of P_i even 47 % and for the other metabolites (GPE, GPC, γ -, α - and β -ATP) between 12 and 16 %. Since these measurements were performed on different volunteers a comparison is difficult and high variations are common.

4.1.2 Pulse Adjustment

Since there is no PCr in liver and the results of subsection 3.1.2 show that its suppression is highest with the RECT600 pulse with reference voltage above 200 V this pulse was chosen for excitation. From the metabolic maps it can be deduced that with rising pulse amplitude the penetration is deeper but gets also more inhomogeneous. By adjusting 90° flip angles in the calibration reference with approx. 135 V pulse amplitude it is estimated based on Biot–Savart law that 300 V are needed to achieve 90° flip angles in 7 cm distance perpendicular to the coil. This is the optimal setting for liver measurements and was therefore selected as excitation pulse amplitude of choice. A coincidental advantage is the half sphere with suppressed signal spreading into the subject: In case it overlaps with the muscle tissue of a volunteer unwanted PCr signal is prevented additionally.

As described in subsection 2.2.2 Pulse Adjustment correction factors for the nonuniform excitation profile were calculated voxel dependent of a VOI. These could not be used directly since

¹with 10 or 18 T_r times or a combination of both

that measurements were performed without a holder where the calibration reference was placed beyond the surface coil. So the distance between the reference and the phantom was larger. Since the 3D-CSI grid placement for the measurement was based on the calibration reference the phantom is located in a different area in that grid. Consequently, a mean value of the voxel dependent factors was calculated to correct for the nonuniform excitation profile.

4.1.3 Positioning of the Calibration Reference

The signal integral of the calibration reference shows a strong dependence on its depth towards the surface coil (subsection 3.1.3). This is caused by the decreasing field strength with distance from the coil center. But also deviations in the yz -plane (translations in plane of the scanner table) could lead to a change in the signal integral of the calibration reference due to B_1 inhomogeneity of the coil. These variations do not only influence the correction for coil loading but also the subject's position in the 3D-CSI grid. The reason for that is the orientation and placement of the grid according to the calibration reference. So if the calibration reference has a shift in any direction it will appear in the same voxel(s) in the CSI but the coil will be on a different location which influences the B_1 field distribution and the correction for that inhomogeneity will be simply wrong compared to a 'correctly' placed measurement.

These results lead to the use of a holding device which keeps the calibration reference in place in reference to the surface coil. The previous discussed issue about different placements of the coil in the 3D-CSI grid and its resulting field distribution is thereby solved. The variations of signal integrals decreased by the use of a holder as well (Table 3.1). While without holder phantom measurements showed standard deviations of above 10 % (15 mmol/L, or even 15 % for the 25 mmol/L phantom) the use of a holder (2nd generation holder) reduced these to below 4 %. While there were only two successive measurements in vivo two series with holder showed a standard deviation of roughly about 50 % and above (#4 and #5). A third one resulted in only 2.6 % probably by coincidence. The signal integrals of the three series which were measured with a holder lead to standard deviations of below 10 % (#1, #2 and #3). Therefore, using a holder reduces the variations in signal integrals of the calibration reference strongly. By looking at the distances of the reference to the subject one might realize that the in vivo measurements and the phantom measurements differ by 2 mm if a holder is used. This is caused by the bottom profile of the phantom which is not plain but has heightening in the center area. In contrast to that comparing these values without the use of a holder the difference is much higher and cannot be explained by the bottom profile of the phantom. It might be explained rather more by compression of the cushions on the scanner table due to the weight of the volunteer and therefore decreasing the distance to the calibration reference (which was fixed in between two cushions). With the use of the incompressible holding device that is no more an issue.

But the holder brings also an unwanted disadvantage: The resonance of the calibration reference shows up two peaks instead of just one. The assumption that these two peaks result in the same signal integral like a measurement without holder with the reference placed in the same position as with holder could not be confirmed even within a standard deviation of 15 %. For a proper fitting of these two resonances in jMRUI an additional line was selected in AMARES. That means that instead of using two lines like for fitting a single resonance the double peak was

fitted by three lines as described in subsection 2.2.3. Due to this additional line there is more freedom in the fitting procedure which could result in higher variations.

For analyzing what causes the splitting up of the resonance of the calibration reference B_0 field maps were recorded (Figure 3.8). As already mentioned while there was no holder used the B_0 distribution seems very smooth and homogeneous but with holder phase wrappings appear. Dielectric pads could not improve these issues probably because they could not be placed to close around the calibration reference since it was almost completely surrounded by the holder.

4.2 Absolute Quantification

4.2.1 Phantom Testing

Since the two phantoms showed comparable metabolic maps (Figure 3.9) they were suitable for validation: This was performed with and without the use of a Hamming filter. The results for the latter showed for the 100 quantified voxels a mean value of 26.12 mmol/L phosphorus which is close to the actual concentration of 25 mmol/L. Despite that, the standard deviation was quite high with 4.11 mmol/L which is also visible in Figure 3.10 on the right side, top right. The factor for the coil load correction ($\frac{I_{ref}(p)}{I_{ref}}$) was about 0.89. In contrast to that by using a Hamming filter the mean concentration was underestimated with a value of 21.86 mmol/L but the standard deviation was reduced to 2.13 mmol/L. The metabolic maps shows a much smoother concentration distribution (Figure 3.10 right side, bottom right). The coil load correction factor was lower with 0.87 compared to the unfiltered quantification. The variation of this correction factor cannot explain the difference in the calculated mean concentrations. The reason might result though from the higher fitting freedom due to the use of three lines for fitting the double resonance of the calibration reference. Another possibility could be different shimming settings leading to small variations in the resonances of the calibration reference. The homogeneity of the absolute quantification (Figure 3.10 right side, top and bottom right) is dependent on the different jMRUI fitting of the phantom resonance of both the validation as well as the correction phantom. Figure 4.1 shows the original spectrum of a central voxel, its fitted peak and the residual spectrum. The latter one should be only noise but still contains some signal. Applying a Hamming filter reduces that residual signal but does not prevent it completely. This might be the reason why the filtered quantification is more homogeneous than the unfiltered.

4.2.2 Hamming Filter

The signal integral map (Figure 3.11, left) shows how data of a small source like the calibration reference is influenced by the PSF. This is very similar to the theoretical PSF of a point source of Figure 1.4, bottom right. Focusing on one column through the calibration reference the same is visible in 1D (cf. Figure 3.11, right with Hamming 0 % and Figure 1.4, bottom left). Applying a 50 % Hamming filter on those data reduces the signal and suppresses the first side lobes by about half. The FWHM gets slightly stretched. For omitting the side lobes as good as possible a 100 % Hamming filter should be applied. This leads to further line broadening and signal reduction but prevents voxel bleeding caused by the side lobes of the PSF. The thereby increased voxel size is accepted due to the benefits the Hamming filter achieves. The latter is exemplified by comparing an unfiltered and filtered spectrum originating from the same voxel: From Figure 3.12 it can be seen that the Hamming filter suppresses one peak at 0 ppm. Since the spectra originate from a voxel located in the liver there should be no PCr signal (0 ppm) visible. That means that this signal of the unfiltered spectrum appears due to voxel bleeding and should be omitted. By using a Hamming filter many more voxels located in the liver fulfill the desired conditions for absolute quantification like very low PCr signal and proper SNR and therefore can be used for calculation of a mean value.

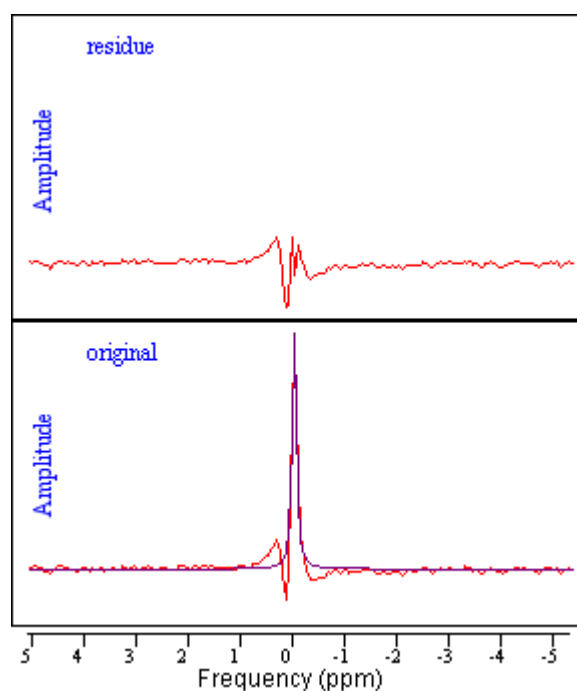


Figure 4.1: jMRUI fitting of a spectrum originating from a central voxel ($x = 8, y = 8, z = 7$) of the correction phantom; bottom: original spectrum (red) overlaid with fitting function (blue); top: residual spectrum.

4.2.3 Quantification Results in Vivo

Comparing the results of Table 3.3 with previous metabolite determinations like from M. Chmelík et al. (2008) [9] or from A. Laufs et al. (2014) [12] (Table 1.3) it is clear that there is a huge underestimation when no holder is used. This might be caused due to different distances of the calibration reference between phantom and in vivo measurements. In subsection 3.2 it is mentioned that this variation is about 5 mm (cf. Table 3.1). It could be caused due to compression of the cushions on the scanner table as explained in subsection 4.1.3.

Figure 4.2 shows the comparison of the results with holder and Hamming filtered of Table 3.2 with the studies listed in Table 1.3. Thereby the PME column is the sum of the PC and the PE signal and the PDE column consists of GPC and GPE. Although PtdC should as well be included in PDE it was not added since its T_1 time in the liver is unknown at 7 T and therefore no saturation correction could be performed. γ - and α -ATP match well with the results of A. Laufs et al. (2014) [12] whereas γ -ATP according to M. Chmelík et al. (2008) [9] is a bit lower. The determined P_i concentration in this study is between the other two studies and PME value is slightly higher than calculated by the compared studies. For the PDE concentration the results of M. Chmelík et al. (2008) [9] and A. Laufs et al. (2014) are already quite different. The presented PDE results of this study is below the other two but with 1 mmol/L deviation close to that of A. Laufs et al. (2014) and it does not contain the PtdC concentration as already mentioned.

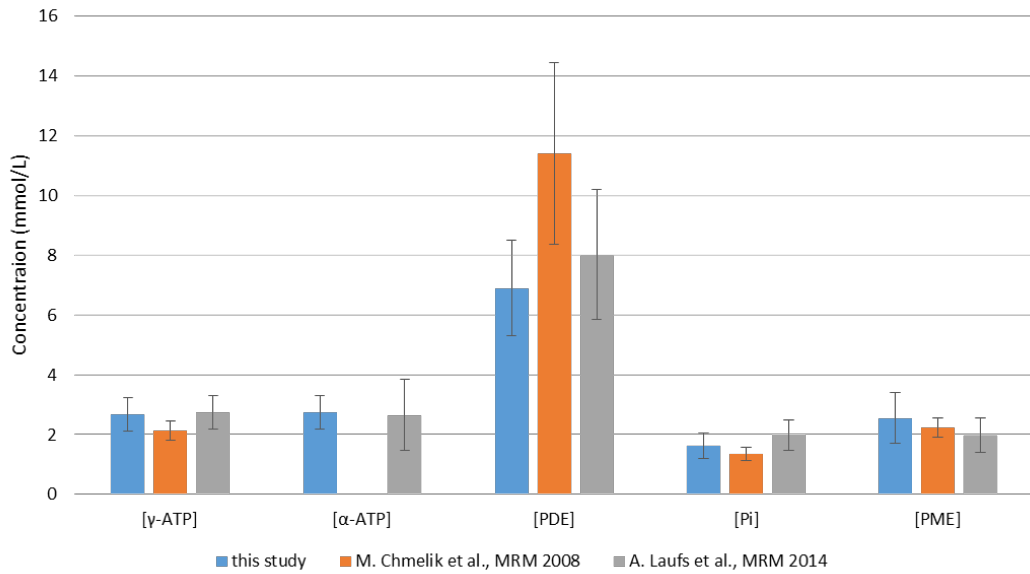


Figure 4.2: Comparison of presented results (Table 3.2) with other studies (M.Chmelik et al. (2008) [9], A.Laufs et al. (2014) [12]) (this study: [PDE] = [GPC] + [GPE] ([PtdC] not included due to unknown T_1 at 7 T), [PME] = [PC] + [PE]).

An example of the jMRUI fitting is depicted in Figure 3.14. β -ATP concentration was not calculated since it could not be brought into phase with the other metabolites. Also signal of the calibration reference is around the same frequency range and might reach due to some errors into the liver. Instead of small resonances as UDPG, NADH and PtdC jMRUI might fit some noise around these lines if SNR is too low. Another problem is that it is quite difficult to phase the spectra. The residual spectrum should contain only noise but in addition its baseline is lower in frequency ranges of many metabolites close to each other and it shows signals where the fitting was not performed well possibly caused by wrong phasing.

Summary & Conclusion

The phantom validation with the use of a Hamming filter shows already that the method presented by M. Chmelík et al. (2008) [9] leads also at magnetic high fields of 7 T to a stable B_1 inhomogeneity correction although there is some underestimation left which still needs some further investigation: A more stable coil load calibration could correct for that issue. If the splitting of the peaks is prevented the fitting could be achieved with less parameters and less freedom and therefore lower possible variations. For metabolites far off resonance the correction for the nonuniform excitation pulse profile is more accurate if the correction phantom is measured at same offset frequency and not by applying a single factor for the whole 3D-CSI grid. Despite that the results of the absolute quantification show comparable concentrations to previous studies ([9] and [12]). The increase of the field strength leads to better spectral resolution and the distinction of the PC and PE signal (at 3 T only one peak, PME) as well as the GPC, GPE and PtdC signal (at 3 T only one peak, PDE). Additional NADH and UDPG can be detected. This can be useful when analyzing hepatic metabolism on a microscopic basis. More information about microbiological and chemical processes due to concentration changes caused by metabolic dysfunctions can be gained. Therefore specific liver disorders can be understood better and highly adapted therapy could be provided.

APPENDIX **A**

Detailed Results

Table A.1: Weighted mean based on signal intensity in mmol/L of single measurements of 3 volunteers (# 1-3) with each 2 successive measurements (# no.1-2) with the use of a holder.

subject	voxels	factor	$[\gamma\text{-ATP}]$	$[\alpha\text{-ATP}]$	[GPC]	[GPE]	[PtdC] ¹	[P _i]	[PC]	[PE]	[UDPG] ¹	[NADH] ¹
# 1.1	68	0.93	3.0832	3.1389	3.4291	4.4405	0.3360	1.9170	1.6768	1.4639	0.2136	0.2722
# 1.2	61	1.02	3.4431	3.2451	3.7938	4.2505	0.2784	2.1743	1.6646	1.6987	0.3343	0.4226
# 2.1	46	0.69	2.8178	3.0092	2.8460	4.1375	0.2434	1.8635	1.6306	1.6951	0.2225	0.3422
# 2.2	27	0.59	2.6188	2.9699	1.7887	2.5749	0.1010	1.3502	0.8241	1.2169	0.1979	0.1746
# 3.1	58	0.62	2.0001	2.0506	3.8765	3.2798	0.2687	1.3166	1.1105	0.7833	0.1093	0.2741
# 3.2	72	0.63	2.1207	2.0269	3.9634	3.0004	0.4428	1.1069	1.0296	0.5492	0.1092	0.1534

Table A.2: Weighted mean based on signal intensity in mmol/L of single measurements of 3 volunteers (# 4-6) with each 2 successive measurements (# no.1-2) without the use of a holder and without Hamming filter.

subject	voxels	factor	$[\gamma\text{-ATP}]$	$[\alpha\text{-ATP}]$	[GPC]	[GPE]	[PtdC] ¹	[P _i]	[PC]	[PE]	[UDPG] ¹	[NADH] ¹
# 4.1	20	0.49	1.5490	1.9759	1.7716	1.9890	0.4106	1.0567	1.1249	0.5233	0.2271	0.3543
# 4.2	20	0.12	0.5730	0.5068	0.6404	0.6048	0.0473	0.3880	0.2972	0.2358	0.0688	0.2110
# 5.1	18	0.30	0.9980	1.5707	0.7144	1.2817	0.0952	0.4022	0.2402	0.3669	0.0540	0.1096
# 5.2	23	0.71	2.0723	1.9843	1.7314	3.0964	0.1964	0.9911	0.7285	0.7244	0.1844	0.2891
# 6.1	32	0.30	0.9362	1.0623	1.0991	1.1229	0.1711	0.6343	0.6478	0.3835	0.0460	0.0951
# 6.2	24	0.29	0.8164	0.7416	1.0563	1.3507	0.1165	0.5670	0.4477	0.3021	0.0553	0.1224

¹no saturation correction due to missing T_1 of these metabolites at 7 T

Bibliography

- [1] R.A. de Graaf. *In Vivo NMR Spectroscopy: Principles and Techniques*. Wiley, 2007. ISBN 9780470026700.
- [2] D.G. Gadian. *NMR and its Applications to Living Systems*. Oxford science publications. OUP Oxford, 1996. ISBN 9780198558033.
- [3] M.A. Bernstein, K.F. King, and X.J. Zhou. *Handbook of MRI pulse sequences*. Elsevier, 2004. ISBN 9780120928613.
- [4] R. Freeman. *Magnetic Resonance in Chemistry and Medicine*. Ill., graph. Darst. Oxford University Press, 2003. ISBN 9780199262250.
- [5] M. Chmelík. *Three-dimensional Magnetic Resonance Spectroscopic Imaging for Absolute Quantification of In Vivo ³¹P Metabolites in Human Liver*. PhD thesis, Medical University of Vienna, 2009.
- [6] A. Skoch, F. Jiru, and J. Bunke. Spectroscopic imaging: basic principles. *Eur J Radiol*, 67(2):230–239, Aug 2008. doi: 10.1016/j.ejrad.2008.03.003.
- [7] R.W. Prost. Magnetic resonance spectroscopy. *Med Phys*, 35(10):4530–4544, Oct 2008. doi: 10.1118/1.2975225.
- [8] A.I. Schmid, M. Chmelík, J. Szendroedi, M. Krssák, A. Brehm, E. Moser, and M. Roden. Quantitative ATP synthesis in human liver measured by localized ³¹P spectroscopy using the magnetization transfer experiment. *NMR Biomed*, 21(5):437–443, Jun 2008. doi: 10.1002/nbm.1207.
- [9] M. Chmelík, A.I. Schmid, S. Gruber, J. Szendroedi, M. Krššák, S. Trattnig, E. Moser, and M. Roden. Three-dimensional high-resolution magnetic resonance spectroscopic imaging for absolute quantification of ³¹P metabolites in human liver. *Magn Reson Med*, 60(4): 796–802, Oct 2008. doi: 10.1002/mrm.21762.
- [10] M. Chmelík, M. Považan, M. Krššák, S. Gruber, M. Tkačov, S. Trattnig, and W. Bogner. In vivo (³¹P) magnetic resonance spectroscopy of the human liver at 7 T: an initial experience. *NMR Biomed*, 27(4):478–485, Apr 2014. doi: 10.1002/nbm.3084.

- [11] M. Chmelík, L. Valkovič, P. Wolf, W. Bogner, M. Gajdošík, E. Halilbasic, S. Gruber, M. Trauner, M. Krebs, S. Trattnig, and M. Krššák. Phosphatidylcholine contributes to in vivo (31)P MRS signal from the human liver. *Eur Radiol*, 25(7):2059–2066, Jul 2015. doi: 10.1007/s00330-014-3578-y.
- [12] A. Laufs, R. Livingstone, B. Nowotny, P. Nowotny, F. Wickrath, G. Giani, J. Bunke, M. Roden, and J.H. Hwang. Quantitative liver 31P magnetic resonance spectroscopy at 3T on a clinical scanner. *Magn Reson Med*, 71(5):1670–1675, May 2014. doi: 10.1002/mrm.24835.
- [13] P.A. Hasgall, F. Di Gennaro, C. Baumgartner, E. Neufeld, M.C. Gosselin, D. Payne, A. Klingeböck, and N. Kuster. *IT'IS Database for thermal and electromagnetic parameters of biological tissues*. Version 2.6, Jan 13th 2015. URL www.itis.ethz.ch/database. [accessed: Jun 18th 2015].
- [14] A. Naressi, C. Couturier, J. M. Devos, M. Janssen, C. Mangeat, R. de Beer, and D. Graveron-Demilly. Java-based graphical user interface for the MRUI quantitation package. *MAGMA*, 12(2-3):141–152, May 2001.
- [15] Vanhamme, van den Boogaart A, and Van Huffel S. Improved method for accurate and efficient quantification of MRS data with use of prior knowledge. *J Magn Reson*, 129(1): 35–43, Nov 1997.

List of Figures

1.1	Sphere with spin in a magnetic field	5
1.2	Spin ensemble in a rotating frame	7
1.3	Complex FID signal	11
1.4	1D and 2D PSF with rectangular and circular k-space sampling	14
1.5	Frequency range of phosphorus metabolites	14
1.6	In vivo ³¹ P NMR spectrum of liver at 3 T	15
2.1	7 T system and surface coil	19
2.2	Phantom, calibration reference and holding devices	20
2.3	Experimental setup	23
2.4	Localizer images with preparation settings	24
2.5	IDL tool	27
3.1	Comparison of RECT and AHP spectra at different pulse amplitudes	30
3.2	Evolution of signal integrals of RECT and AHP spectra with pulse amplitude	30
3.3	Evolution of 3D-CSI maps with increasing pulse amplitude	31
3.4	Simulated signal distribution in human body	31
3.5	Calculated correction factors for nonuniform excitation profile	32
3.6	Variation of signal integrals of calibration reference with distance	32
3.7	Peak splitting of calibration reference due to holder	34
3.8	Field maps of calibration reference without and with holder	34
3.9	3D-CSI maps of phantoms with different concentrations	35
3.10	Phantom validation	36
3.11	Measured PSF and effect of Hamming filter	36
3.12	Effect of Hamming filter on spectra	37
3.13	Voxels for in vivo quantification	37
3.14	jMRUI fitting of in vivo spectrum	38
4.1	jMRUI fitting of phantom spectrum	45
4.2	Comparison of absolute quantifications	46

List of Tables

1.1	NMR characteristics of nuclei	6
1.2	T_1 times of hepatic metabolites at 7 T	16
1.3	Measured phosphorus concentrations in liver	17
3.1	Comparison of signal integrals of calibration reference without and with holder . .	33
3.2	Absolute concentrations	37
3.3	Absolute concentrations without usage of holder	39
A.1	Absolute concentrations of the single measurements with holder	50
A.2	Absolute concentrations of the single measurements without holder	50